

Title:

Wave power extraction from multiple oscillating water columns along a straight coast

Journal:

Journal of Fluid Mechanics

Author names and affiliations:

Siming Zheng^{1,*}, Alessandro Antonini², Yongliang Zhang³, Deborah Greaves¹, Jon Miles¹, Gregorio Iglesias^{4,1}

1 School of Engineering, University of Plymouth, Drake Circus, Plymouth PL4 8AA, United Kingdom

2 Department of Hydraulic Engineering, Delft University of Technology, The Netherlands

3 State Key Laboratory of Hydrosience and Engineering, Tsinghua University, Beijing, 100084, China

4 Centre for Marine Renewable Energy Ireland (MaREI), Environmental Research Institute & School of Engineering, University College Cork, Ireland

* Email address for correspondence: siming.zheng@plymouth.ac.uk

<https://doi.org/10.1017/jfm.2019.656>

Received 20 March 2019; revised 6 August 2019; accepted 6 August 2019

Wave power extraction from multiple oscillating water columns along a straight coast

Siming Zheng¹†, Alessandro Antonini², Yongliang Zhang³,
Deborah Greaves¹, Jon Miles¹, and Gregorio Iglesias^{4,1}

¹School of Engineering, University of Plymouth, Drake Circus, Plymouth PL4 8AA, United Kingdom

²Department of Hydraulic Engineering, Delft University of Technology, The Netherlands

³State Key Laboratory of Hydrosience and Engineering, Tsinghua University, Beijing, 100084, China

⁴Centre for Marine Renewable Energy Ireland (MaREI), Environmental Research Institute & School of Engineering, University College Cork, Ireland

(Received xx; revised xx; accepted xx)

The integration of oscillating water column (OWC) wave energy converters into a coastal structure (breakwater, jetty, pier, etc.) or, more generally, their installation along the coast is an effective way to increase the accessibility of wave power exploitation. In this paper, a theoretical model is developed based on the linear potential flow theory and eigenfunction matching method to evaluate the hydrodynamic performance of an array of OWCs installed along a vertical straight coast. The chamber of each OWC consists of a hollow vertical circular cylinder, which is half embedded in the wall. The OWC chambers in the theoretical model may have different sizes, i.e., different values of the radius, wall thickness and submergence. At the top of each chamber, a Wells turbine is installed to extract power. The effects of the Wells turbine together with the air compressibility are taken into account as a linear power take-off system. The hydrodynamic and wave power extraction performance of the multiple coast-integrated OWCs is compared with that of a single offshore/coast-integrated OWC and of multiple offshore OWCs. More specifically, we analyse the role of the incident wave direction, chamber size (i.e., radius, wall thickness and submergence), spacing between OWCs and number of OWCs by means of the present theoretical model. It is shown that wave power extraction from the coast-integrated OWCs for a certain range of wave conditions can be significantly enhanced due to both the constructive array effect and the constructive coast effect. (doi:10.1017/jfm.2019.656)

Key words: wave-structure interactions, surface gravity waves, wave scattering

1. Introduction

Many different concepts for wave energy conversion have been proposed (Clément *et al.* 2002; Drew *et al.* 2009; Rusu & Onea 2018). However, compared with other renewable energy technologies, such as solar, wind or tidal, wave power is rather immature, and relatively few wave energy converters (WECs) have achieved fully commercial operation (Astariz & Iglesias 2015; Drew *et al.* 2009; Mustapa *et al.* 2017).

† Email address for correspondence: siming.zheng@plymouth.ac.uk

39 Among the various wave energy conversion concepts, the oscillating water column
40 (OWC) is probably the most extensively investigated and best developed (Falcão &
41 Henriques 2016; Heath 2012). An OWC is generally composed of a hollow chamber with
42 its bottom open to the sea below the waterline. Subjected to ocean waves, the water
43 column enclosed by the chamber moves up and down, applying pressure on the air within
44 the chamber. The air is forced in and out of the chamber through a turbine installed at
45 the top of the OWC, allowing for power extraction.

46 The cost of power is the major limitation to the uptake of WECs in commercial
47 operation (Heath 2012; Di Lauro *et al.* 2019). This is a general issue with wave energy,
48 not specific to OWC technology. A number of efforts have been made to achieve com-
49 mercialization of OWCs (Pawitan *et al.* 2019; Viviano *et al.* 2016). The integration of
50 OWCs into coastal structures, such as breakwaters, jetties and piers or along sections of
51 the coast, presents an effective way to increase significantly the attractiveness of wave
52 power exploitation. The fact that the capture factor of WECs may be enhanced by their
53 deployment along the coast (which may be referred to, for simplicity, as the coast effect)
54 was reported for flap-type WECs by Sarkar *et al.* (2015); Michele *et al.* (2016), and
55 also for oscillating buoys by Evans (1988); Zhao *et al.* (2018); Zhang & Ning (2019). In
56 this way, the economics of the OWC can be enhanced thanks to cost-sharing benefits,
57 including construction, installation and maintenance (Arena *et al.* 2017; Boccotti 2007;
58 Heras-Saizarbitoria *et al.* 2013; Mustapa *et al.* 2017). Reliability and survivability of the
59 OWC can be improved as well, allowing power extraction during large wave conditions.

60 Many theoretical investigations have been devoted to wave power extraction by
61 coast/breakwater-integrated OWCs. Evans & Porter (1995) proposed a two-dimensional
62 (2-D) theoretical model to study the performance of an onshore OWC device that
63 consists of a thin vertical surface-piercing lip in front of a vertical wall. It was illustrated
64 that, by choosing proper submergence of the lip and the spacing distance between the lip
65 and the wall, the incident wave power can be captured efficiently. The performance of a
66 thin-walled OWC installed either at the tip of a thin fixed breakwater or along a straight
67 coast was considered by Martins-Rivas & Mei (2009*a,b*), who developed theoretical
68 models based on the linear potential flow theory to solve the three-dimensional (3-D)
69 wave radiation/diffraction problems. To deal with the singular behaviours in the velocity
70 field across the gap under the thin wall of OWC chamber, an integral equation for the
71 horizontal velocity under the wall was employed in their models. The extracted power
72 of the OWC at the tip of a thin breakwater was found to be reasonably insensitive to
73 the incident wave direction, whereas the response of the OWC installed on a straight
74 coast was strongly dependent on wave direction. The best performance occurred under
75 normal incidence for most frequencies. Wave reflection at the coast means that the power
76 captured by the OWC can be doubled. Lovas *et al.* (2010) extended the theoretical
77 model by Martins-Rivas & Mei (2009*a,b*) into a more general model that can be applied
78 to more complex situations, i.e., a thin-walled OWC installed at a coastal corner. The
79 captured power by the OWC at a concave corner was found to be significantly greater
80 than that when the OWC was installed at the tip of a convex corner of right angle.

81 More recently, Zheng *et al.* (2019) developed a theoretical model of a coast/breakwater-
82 integrated OWC, in which the effect of the thickness of the OWC chamber wall was
83 considered. Subjected to a fixed outer radius, the thinner the chamber wall, the larger
84 and broader the main peaks of the frequency response of wave power capture width.
85 Numerical and physical studies on a coast/breakwater-integrated OWC can be found in
86 (Elhanafi *et al.* 2016; Falcão *et al.* 2016; He *et al.* 2012, 2017; Howe & Nader 2017; López &
87 Iglesias 2014; López *et al.* 2016; Morris-Thomas *et al.* 2007; Zhang *et al.* 2012). However,
88 most of these studies are focused on 2-D problems, and therefore miss fundamental

89 dynamics related to direction changes in wave diffraction and radiation from complex-
90 shaped structures.

91 In order to fully harness the available wave power in a region and to produce large
92 quantities of energy for electrical grids, wave farms, i.e., arrays of OWCs, are likely
93 to be deployed. For these OWCs deployed not far away from each other, cost-sharing
94 benefits of installation and electrical power transmission can be made as well. On the
95 basis of an analytical solution of hydrodynamic problems from an oscillating circular
96 patch on the water surface, Nihous (2012) presented a model to predict wave power
97 absorption from an array of OWCs. The OWC chamber was assumed to have a sufficiently
98 shallow draught; thus diffraction effects were neglected in the model. A finite array of
99 fixed OWCs without the restriction of shallow draught was considered by Nader *et al.*
100 (2012) by applying a 3-D finite element method model. The complexity of hydrodynamic
101 interactions between the OWCs within the array was highlighted. Later, a more realistic
102 model with the air compressibility inside the OWC chamber taken into account was
103 proposed (Nader *et al.* 2014; Sarmiento & Falcão 1985; López *et al.* 2019). The results
104 showed that for some certain wave frequencies, more power can be harnessed by the array
105 of fixed OWCs compared with the total power that the same number of OWCs working in
106 isolation could extract. Recently, Konispoliatis & Mavrakos (2016) developed an efficient
107 theoretical model to investigate the performance of an array of free-floating OWCs. Major
108 improvements in terms of extracted power were demonstrated for arrays with certain
109 spacings between the OWCs. More recently, the hydrodynamic characteristics of a hybrid
110 wave farm consisting of both OWCs and point-absorber WECs were investigated by
111 Zheng *et al.* (2018).

112 Apart from the integration of OWCs into coastal structures and the deployment of
113 OWCs in an array, various studies have also been carried out on the development of
114 individual OWCs (Elhanafi *et al.* 2017; Henriques *et al.* 2016; Kurniawan *et al.* 2017;
115 López *et al.* 2014; Ning *et al.* 2018; Pereiras *et al.* 2015; Sheng & Lewis 2018; He *et al.*
116 2019).

117 To the authors' knowledge, most of the previous research work on OWCs has been
118 focused on the investigation of either a single coast-integrated/offshore OWC or an
119 array of offshore OWCs. In this article, the concept of integrating multiple OWCs into a
120 straight coast is proposed. The chamber of each OWC mainly consists of a hollow vertical
121 circular cylinder, which is cut away such that it is half open to the sea from a finite
122 submergence to the seabed. To evaluate the hydrodynamic performance of these coast-
123 integrated OWCs, a 3-D theoretical model is developed based on the linear potential flow
124 theory and eigenfunction matching method. The water depth is assumed to be constant,
125 in order to simplify the wave conditions. The effect of a Wells turbine installed at the top
126 of each OWC together with the air compressibility are taken into account by means of
127 a linear power take-off (PTO) system. Different from most of the previous reviewed 3-D
128 theoretical models for a single coast-integrated thin-walled OWC, the present model can
129 be used to study wave power extraction from multiple coast-integrated OWCs without
130 the thin-wall restriction, i.e., the effect of the wall thickness of the OWC chamber is
131 taken into consideration. The performance of the multiple coast-integrated OWC system
132 is compared with that of a single individual coast-integrated OWC, and also with that
133 of single and multiple offshore OWCs, which consists of a stationary hollow vertical
134 cylinder located in the open sea with the whole cylinder cut off at a finite distance from
135 the seabed. The theoretical model is applied to explore the influences of incident wave
136 direction, chamber size (i.e., radius, wall thickness and submergence), spacing distance
137 between the OWCs and the number of OWCs on power extraction systematically.

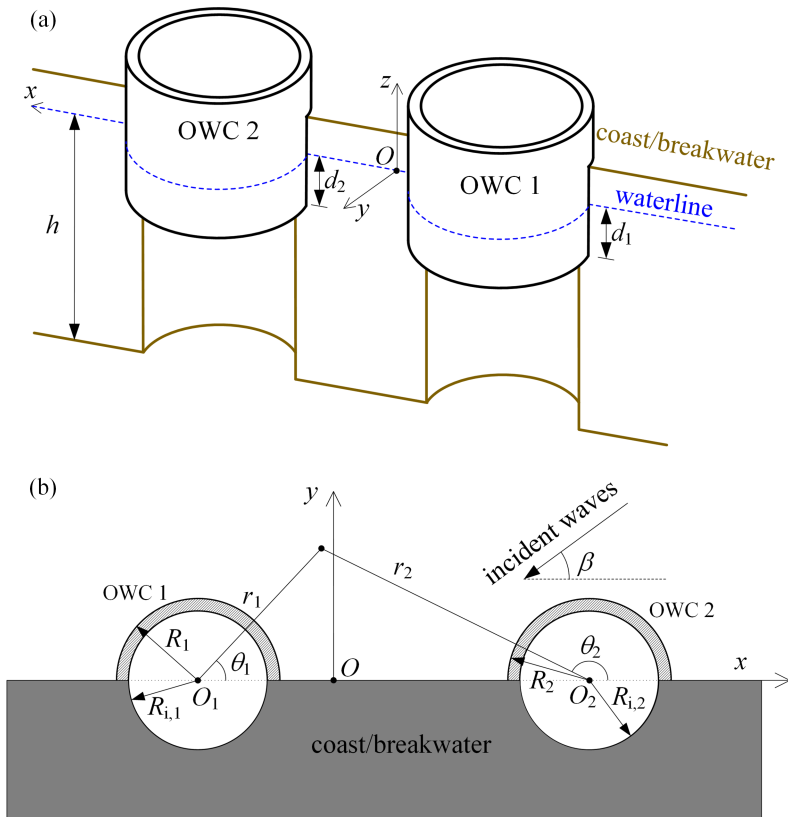


FIGURE 1. Definition sketch: (a) general layout of a pair of OWCs; (b) plan section with key dimensions.

2. Mathematical model

138

139 In the model, a number (N) of OWCs are conceptually installed along a straight coast
 140 in water of finite depth h (see figure 1, where $N = 2$ is taken as an example). A global
 141 Cartesian coordinate system $Oxyz$ is adopted with the Oxy plane at the mean water level
 142 and the Oxz plane at the sidewall of the coast. For the N vertical circular OWC chambers,
 143 the OWCs are numbered along the Ox axis in ascending order, and N local cylindrical
 144 coordinate systems, $O_n r_n \theta_n z_n$, are defined with their origins O_n at the central vertical
 145 axis of the n -th OWC ($n = 1, 2, \dots, N$). The O_n can be defined in Cartesian coordinate
 146 system $Oxyz$ as $(x_n, 0, 0)$. In addition, R_n , $R_{i,n}$ and d_n denote the outer radius, inner
 147 radius and submergence of the n -th OWC chamber, respectively; and D_n represents the
 148 distance between O_n and O_{n+1} .

149 For the coast-integrated OWCs subjected to regular incident waves with small wave
 150 steepness propagating in the direction of β relative to the coast (see figure 1), in the
 151 framework of linear potential flow theory, the fluid flow in the water domain is described
 152 by the velocity potential

$$\phi(x, y, z, t) = \text{Re}[\Phi(x, y, z)e^{-i\omega t}]. \quad (2.1)$$

153 Here Φ is a complex spatial velocity potential independent of time, which needs to satisfy
 154 Laplace's equation in the fluid, in addition to certain linear boundary conditions, which
 155 will be given shortly; i is the imaginary unit; ω denotes the circular frequency of incident
 156 waves; and t is the time. The linear potential flow theory is not suitable for extreme

157 waves, given that it does not account for either the viscous effect or the nonlinear wave
158 dynamics.

159 Under linear theory, the spatial velocity potential Φ may be decomposed as the sum
160 of scattering and radiation potentials, i.e.,

$$\Phi = \Phi_0 + \sum_{n=1}^N p_n \Phi_n, \quad (2.2)$$

161 where Φ_0 is the scattering spatial velocity potential representing the wave field when the
162 coast-integrated OWCs with the top of each chamber entirely open to the air (i.e., no
163 dynamic air pressure) are subjected to the incident waves; p_n is the complex air pressure
164 amplitude inside the n -th OWC chamber; and Φ_n represents the spatial velocity potential
165 due to a unit air pressure oscillation inside the n -th OWC chamber while all the others
166 are at rest.

167 Outside the OWCs Φ_0 can be taken as the sum of two parts, $\Phi_0 = \Phi_I + \Phi_D$, where Φ_I is
168 the spatial velocity potential representing the wave field due to the incident waves in the
169 absence of OWCs, which includes both the incident plane wave and a plane wave reflected
170 by the wall, and Φ_D is the diffracted spatial velocity potential due to the presence of the
171 OWCs. In the n -th local cylindrical coordinate system $O_n r_n \theta_n z$, Φ_I can be written as
172 (Zheng & Zhang 2015)

$$\Phi_I(r_n, \theta_n, z) = -\frac{2igA}{\omega} \frac{Z_0(z)}{Z_0(0)} e^{-ik_0 x_n \cos\beta} \sum_{m=0}^{\infty} \varepsilon_m (-i)^m J_m(k_0 r_n) \cos(m\beta) \cos(m\theta_n). \quad (2.3)$$

173 Here A is the amplitude of incident waves; g denotes the gravitational acceleration; $\varepsilon_m = 1$
174 for $m=0$, whereas $\varepsilon_m = 2$ for $m > 0$; k_0 is the wavenumber, which satisfies the dispersion
175 relation $\omega^2 = gk_0 \tanh(k_0 h)$; J_m denotes the Bessel function of order m ; and $Z_0(z)$ is an
176 eigenfunction given by

$$Z_0(z) = N_0^{-1/2} \cosh[k_0(z+h)], \quad N_0 = \frac{1}{2} \left[1 + \frac{\sinh(2k_0 h)}{2k_0 h} \right]. \quad (2.4)$$

177 The governing equation in the water domain, the free-surface boundary conditions,
178 and the body boundary conditions that Φ_χ ($\chi = 0, 1, 2, \dots, N$) should satisfy are given as
179 follows:

$$\nabla^2 \Phi_\chi = 0, \quad \text{in water}, \quad (2.5)$$

180

$$\frac{\partial \Phi_\chi}{\partial n} = 0, \quad \text{on all solid boundaries}, \quad (2.6)$$

181

$$\left(\frac{\partial \Phi_\chi}{\partial z} - \frac{\omega^2}{g} \Phi_\chi \right) \Big|_{z=0} = \delta_{\chi,n} \frac{i\omega}{\rho g}, \quad \text{on the water surface inside the } n\text{-th OWC chamber}, \quad (2.7)$$

182

$$\left(\frac{\partial \Phi_\chi}{\partial z} - \frac{\omega^2}{g} \Phi_\chi \right) \Big|_{z=0} = 0, \quad \text{on the water surface outside the } n\text{-th OWC chamber}, \quad (2.8)$$

183 in which $\delta_{\chi,n}$ is the Kronecker delta function, which is equal to 1 when $\chi = n$, and is
184 equal to 0 otherwise; and ρ represents the water density.

185 Additionally, it is required that Φ_D and Φ_χ ($\chi = 1, 2, \dots, N$) are outgoing for $r_n \rightarrow \infty$.

3. Solution of scattering and radiated potentials

3.1. Scattering and radiated spatial potentials in different regions

The general solution of the potential Φ_χ in the region enclosed by the n -th OWC, i.e., $r_n \in [0, R_{i,n}]$, $\theta_n \in [0, 2\pi]$, $z \in [-h, 0]$, is formally expressed as

$$\Phi_{\chi,n}^{\text{in}}(r_n, \theta_n, z) = \sum_{m=-\infty}^{\infty} \sum_{l=0}^{\infty} \frac{\tilde{I}_m(k_l r_n)}{k_l \tilde{I}'_m(k_l R_{i,n})} A_{m,l}^{\chi,n} Z_l(z) e^{im\theta_n} - i \frac{\delta_{\chi,n}}{\rho\omega}. \quad (3.1)$$

Here $A_{m,l}^{\chi,n}$ are the unknown coefficients to be solved;

$$\tilde{I}_m(k_l r_n) = \begin{cases} J_m(k_l r_n), & l = 0 \\ I_m(k_l r_n), & l = 1, 2, 3, \dots \end{cases}, \quad (3.2)$$

in which I_m denotes the modified Bessel function of the first kind of order m ; k_l is the eigenvalue, which is given by (e.g., Falnes (2002))

$$\omega^2 = -gk_l \tan(k_l h), \quad l = 1, 2, 3, \dots, \quad (3.3)$$

and the corresponding eigenfunction $Z_l(z)$ is defined by

$$Z_l(z) = N_l^{-1/2} \cos[k_l(z+h)], \quad N_l = \frac{1}{2} \left[1 + \frac{\sin(2k_l h)}{2k_l h} \right], \quad l = 1, 2, 3, \dots \quad (3.4)$$

The eigenfunctions $Z_0(z)$ and $Z_l(z)$, as given in equations (2.4) and (3.4) form a complete orthogonal set in $z \in [-h, 0]$:

$$\int_{-h}^0 Z_m(z) Z_l(z) dz = h \delta_{m,l}, \quad m, l = 0, 1, 2, 3, \dots \quad (3.5)$$

In the region beneath the n -th OWC chamber wall, i.e., $r_n \in [R_{i,n}, R_n]$, $\theta_n \in [0, \pi]$, $z \in [-h, -d_n]$, the potential Φ_χ can be expressed as

$$\begin{aligned} \Phi_{\chi,n}^{\text{ring}}(r_n, \theta_n, z) = \sum_{m=0}^{\infty} \left[F_{m,0}^{\chi,n}(r_n) + \sum_{l=1}^{\infty} \left(C_{m,l}^{\chi,n} \frac{I_m(\beta_{n,l} r_n)}{I_m(\beta_{n,l} R_n)} \right. \right. \\ \left. \left. + D_{m,l}^{\chi,n} \frac{K_m(\beta_{n,l} r_n)}{K_m(\beta_{n,l} R_n)} \right) \cos[\beta_{n,l}(z+h)] \right] \cos(m\theta_n), \end{aligned} \quad (3.6)$$

which satisfies the no-flux boundary condition on the coast ($\theta_n = 0$ and π). Therein,

$$F_{m,0}^{\chi,n}(r_n) = \begin{cases} C_{m,0}^{\chi,n} + D_{m,0}^{\chi,n} \left[1 + \ln \left(\frac{r_n}{R_n} \right) \right], & m = 0 \\ C_{m,0}^{\chi,n} \left(\frac{r_n}{R_n} \right)^{|m|} + D_{m,0}^{\chi,n} \left(\frac{r_n}{R_n} \right)^{-|m|}, & m \neq 0 \end{cases}, \quad (3.7)$$

in which $C_{m,l}^{\chi,n}$ and $D_{m,l}^{\chi,n}$ are the unknown coefficients to be determined; K_m is the modified Bessel function of the second kind of order m ; and $\beta_{n,l}$ is the l -th eigenvalue given by

$$\beta_{n,l} = \frac{l\pi}{h-d_n}, \quad l = 0, 1, 2, 3, \dots \quad (3.8)$$

In the region outside the OWC chambers and in front of the coast extending towards infinite distance horizontally, i.e., $r_n \in [R_n, \infty]$, $\theta_n \in [0, \pi]$, $z \in [-h, 0]$, the potential Φ_χ

204 can be expressed as

$$\Phi_{\chi}^{\text{out}}(r_n, \theta_n, z) = \delta_{\chi,0} \Phi_{\text{I}} + \sum_{j=1}^N \Phi_{\chi,j}^{\text{out}}, \quad (3.9)$$

205 where $\Phi_{\chi,j}^{\text{out}}$ represents the velocity potential component diffracted/radiated from the j -th
206 OWC and it can be written in the j -th local cylindrical coordinate $O_j r_j \theta_j z$ as

$$\Phi_{\chi,j}^{\text{out}}(r_j, \theta_j, z) = \sum_{m=0}^{\infty} \sum_{l=0}^{\infty} E_{m,l}^{\chi,j} \frac{\tilde{K}_m(k_l r_j)}{\tilde{K}_m(k_l R_j)} \cos(m\theta_j) Z_l(z), \quad (3.10)$$

207 which satisfies the no-flux boundary condition on the coast ($\theta_j = 0$ and π). Here $E_{m,l}^{\chi,j}$
208 are the unknown coefficients to be determined; and

$$\tilde{K}_m(k_l r_j) = \begin{cases} H_m(k_l r_j), & l = 0 \\ K_m(k_l r_j), & l = 1, 2, 3, \dots \end{cases}, \quad (3.11)$$

209 where H_m denotes the Hankel function of the first kind of order m .

210 Following Graf's addition theorem for Bessel functions (Abramowitz & Stegun 1964),

$$\tilde{K}_m(k_l r_j) \cos(m\theta_j) = \sum_{m'=-\infty}^{\infty} \tilde{K}_{m+m'}(k_l R_{jn}) \tilde{I}_{m'}(k_l r_n) e^{i(m\alpha_{jn} + m'\alpha_{nj})} \cos(m'\theta_n), \quad r_n \leq R_{jn}, \quad (3.12)$$

211 where R_{jn} and α_{jn} denote the norm and the angle of vector $\overrightarrow{O_j O_n}$, respectively. Therefore,
212 the expression of $\Phi_{\chi,j}^{\text{out}}$ can be transformed from the j -th local cylindrical coordinate into
213 the n -th one, and equation (3.9) is ultimately expressed in the local cylindrical coordinate
214 $O_n r_n \theta_n z$ by

$$\begin{aligned} \Phi_{\chi}^{\text{out}}(r_n, \theta_n, z) &= \delta_{\chi,0} \Phi_{\text{I}} + \sum_{m=0}^{\infty} \sum_{l=0}^{\infty} E_{m,l}^{\chi,n} \frac{\tilde{K}_m(k_l r_n)}{\tilde{K}_m(k_l R_n)} \cos(m\theta_n) Z_l(z) \\ &+ \sum_{\substack{j=1 \\ j \neq n}}^N \sum_{m=0}^{\infty} \sum_{l=0}^{\infty} \frac{E_{m,l}^{\chi,j} Z_l(z)}{\tilde{K}_m(k_l R_j)} \sum_{m'=-\infty}^{\infty} \tilde{K}_{m+m'}(k_l R_{jn}) \tilde{I}_{m'}(k_l r_n) e^{i(m\alpha_{jn} + m'\alpha_{nj})} \cos(m'\theta_n), \\ &\text{for } r_n \leq R_{jn}. \end{aligned} \quad (3.13)$$

3.2. Method of computation for unknown coefficients

216 It is easy to check that the governing equation and all the boundary conditions given
217 in equations (2.5)-(2.8), except the no-flux condition on the inner and outer cylindrical
218 surfaces of each OWC chamber $r_n = R_n$ and $r_n = R_{i,n}$, have been satisfied by the
219 scattering and radiated spatial potentials in different regions, as expressed in Section
220 3.1, regardless of the values of the unknown coefficients. Note that the no-flux condition
221 at $r_n = R_n$ and $r_n = R_{i,n}$, together with the pressure and velocity continuity conditions
222 on the interfaces of each two adjacent regions should be satisfied as well, which can be
223 applied to solve the unknown coefficients.

224 The continuity conditions for the scattering and radiated spatial potentials are given
225 as follows:

226 (1) Continuity of normal velocity at the boundary $r_n = R_{i,n}$:

$$\frac{\partial \Phi_{\chi,n}^{\text{in}}}{\partial r_n} \Big|_{r_n=R_{i,n}} = \begin{cases} 0, & z \in [-d_n, 0], \theta_n \in [0, \pi]; \\ & \text{and } z \in [-h, 0], \theta_n \in [\pi, 2\pi], \\ \frac{\partial \Phi_{\chi,n}^{\text{ring}}}{\partial r_n} \Big|_{r_n=R_{i,n}}, & z \in [-h, -d_n], \theta_n \in [0, \pi], \end{cases} \quad (3.14)$$

227 (2) Continuity of normal velocity at the boundary $r_n = R_n$:

$$\frac{\partial \Phi_{\chi,n}^{\text{out}}}{\partial r_n} \Big|_{r_n=R_n} = \begin{cases} 0, & z \in [-d_n, 0], \theta_n \in [0, \pi], \\ \frac{\partial \Phi_{\chi,n}^{\text{ring}}}{\partial r_n} \Big|_{r_n=R_n}, & z \in [-h, -d_n], \theta_n \in [0, \pi], \end{cases} \quad (3.15)$$

228 (3) Continuity of pressure at the boundary $r_n = R_{i,n}$:

$$\Phi_{\chi,n}^{\text{ring}} \Big|_{r_n=R_{i,n}} = \Phi_{\chi,n}^{\text{in}} \Big|_{r_n=R_{i,n}}, \quad z \in [-h, -d_n], \theta_n \in [0, \pi], \quad (3.16)$$

229 (4) Continuity of pressure at the boundary $r_n = R_n$:

$$\Phi_{\chi,n}^{\text{out}} \Big|_{r_n=R_n} = \Phi_{\chi,n}^{\text{ring}} \Big|_{r_n=R_n}, \quad z \in [-h, -d_n], \theta_n \in [0, \pi]. \quad (3.17)$$

230 Inserting the expressions of $\Phi_{\chi,n}^{\text{in}}$, $\Phi_{\chi,n}^{\text{ring}}$ and $\Phi_{\chi,n}^{\text{out}}$ as given in Section 3.1 into the above
 231 continuity conditions, i.e., equations (3.14)-(3.17), and making use of the orthogonality
 232 of both trigonometric functions and eigenfunctions, the unknown coefficients $A_{m,l}^{\chi,n}$, $C_{m,l}^{\chi,n}$
 233 and $D_{m,l}^{\chi,n}$ can be determined by solving a linear algebraic system after truncation (Yu
 234 *et al.* 2019; Zheng & Zhang 2015, 2016). For convenience, the details of the derivations
 235 can be found in Appendix A.

3.3. Wave excitation volume flux and hydrodynamic coefficients

236
 237 The upward displacement of the water surface inside the n -th OWC chamber, i.e.,
 238 the wave excitation volume flux of the n -th OWC, induced by scattering waves can be
 239 written as

$$\begin{aligned} Q_e^{(n)} &= \int_0^{2\pi} \int_0^{R_{i,n}} \frac{\Phi_{0,n}^{\text{in}}(r_n, \theta_n, z)}{\partial z} \Big|_{z=0} r_n dr_n d\theta_n \\ &= \frac{2\pi\omega^2 R_{i,n}}{g} \left(-\frac{A_{0,0}^{0,n}}{k_0^2} Z_0(0) + \sum_{l=1}^{\infty} \frac{A_{0,l}^{0,n}}{k_l^2} Z_l(0) \right). \end{aligned} \quad (3.18)$$

240 In a similar way, the volume flux of the n -th OWC due to the radiated velocity
 241 potential induced by the unit air pressure oscillation inside the χ -th OWC chamber
 242 can be evaluated by

$$Q_\chi^{(n)} = \frac{2\pi\omega^2 R_{i,n}}{g} \left(-\frac{A_{0,0}^{\chi,n}}{k_0^2} Z_0(0) + \sum_{l=1}^{\infty} \frac{A_{0,l}^{\chi,n}}{k_l^2} Z_l(0) \right) = -(c_\chi^{(n)} - ia_\chi^{(n)}), \quad (3.19)$$

243 in which $c_\chi^{(n)}$ and $a_\chi^{(n)}$ on the right hand of the second equals sign are the hydrody-
 244 namic coefficients, more specifically, the so-called radiation damping and added mass,
 245 respectively.

246 The method as shown in equation (3.19) is a straightforward way to calculate the
 247 hydrodynamic coefficient, and is referred to here as the direct method. It is worth

noting that there is an alternative approach based on the Haskind relation which can be employed to evaluate $c_\chi^{(n)}$ indirectly (e.g., Falnes (2002); Martins-Rivas & Mei (2009a)),

$$c_\chi^{(n)} = \frac{k}{8\pi\rho g c_g A^2} \int_0^\pi Q_e^{(n)}(\beta) Q_e^{(n)*}(\beta) d\beta, \quad (3.20)$$

where the superscript $*$ denotes complex conjugate, c_g denotes the wave group velocity and k is used to represent k_0 for the sake of simplicity. The Haskind-type identity as given in equation (3.20) links the radiation and scattering problems and presents a way to check the accuracy of the proposed theoretical model.

4. Relation between power take-off system and hydrodynamic problems

4.1. Response of the OWCs

The wave scattering and radiation problems are coupled by the PTO system. Assuming the mass flux through the Wells turbines is proportional to the chamber air pressure and the effect of air compressibility in the chamber is linear, following Sarmiento & Falcão (1985); Martins-Rivas & Mei (2009a,b), the complex air pressure amplitude in each OWC chamber is related to the scattering and radiated velocity potentials, resulting in the following matrix equation:

$$[-i(\mathbf{M}_{\text{PTO}} + \mathbf{M}) + (\mathbf{C}_{\text{PTO}} + \mathbf{C})]\mathbf{p} = \mathbf{Q}_e. \quad (4.1)$$

Here \mathbf{M}_{PTO} is a diagonal matrix of size $N \times N$, adapted to consider the effect of air compressibility, and the n -th element in the diagonal of \mathbf{M}_{PTO} can be expressed as $\omega V_n / (v^2 \rho_0)$, in which V_n is the air chamber volume of the n -th OWC, v denotes the sound velocity in air and ρ_0 represents the static air density; \mathbf{C}_{PTO} is a diagonal matrix of size $N \times N$ as well, and it is used to represent the damping of the PTO system of each OWC, which depends on the rotational speed of the turbines, their specification and design, and also the static air density; \mathbf{M} and \mathbf{C} are two matrices of size $N \times N$ that represent the hydrodynamic coefficients that correspond to $a_\chi^{(n)}$ and $c_\chi^{(n)}$, respectively; and \mathbf{p} is a column vector of length N that includes all the air pressure responses of the multiple OWCs p_n , $n = 1, 2, \dots, N$. The forcing term \mathbf{Q}_e is a column vector of length N including the complex wave excitation volume flux acting on each OWC $Q_e^{(n)}$, $n = 1, 2, \dots, N$.

As \mathbf{M} , \mathbf{C} , and \mathbf{Q}_e have already been theoretically evaluated in the previous sections, and \mathbf{M}_{PTO} and \mathbf{C}_{PTO} are known for a specified PTO system, the response of the OWCs can be easily determined by solving the N th-order complex matrix equation (4.1).

4.2. Wave power extraction

Once the air pressure response in each OWC is obtained, the time-averaged power output by these coast-integrated OWCs can be directly calculated by (e.g., Falnes (2002))

$$P = \frac{1}{2} \mathbf{p}^\dagger \mathbf{C}_{\text{PTO}} \mathbf{p} = \frac{1}{2} \left\| \mathbf{C}_{\text{PTO}}^{1/2} \mathbf{p} \right\|^2, \quad (4.2)$$

where the superscript \dagger denotes complex-conjugate transpose. Since \mathbf{C}_{PTO} is a real diagonal matrix, the second equality holds, in which $\|\cdot\|$ represents the two-norm of a vector.

Following Lovas *et al.* (2010), the dimensionless coefficients of $Q_e^{(n)}$, the hydrodynamic coefficients $c_\chi^{(n)}$ and $a_\chi^{(n)}$, and the corresponding PTO parameters can be defined as

285 follows:

$$\bar{Q}_e^{(n)} = \frac{\sqrt{g/h}}{Ahg} Q_e^{(n)}; \quad (\bar{c}_\chi^{(n)}, \bar{a}_\chi^{(n)}, \bar{c}_{\text{PTO}}^{(n)}, \bar{a}_{\text{PTO}}^{(n)}) = \frac{\rho\sqrt{g/h}}{h} (c_\chi^{(n)}, a_\chi^{(n)}, c_{\text{PTO}}^{(n)}, a_{\text{PTO}}^{(n)}), \quad (4.3)$$

286 with which the time-averaged power absorption as given in equation (4.2) can be rewritten
287 in terms of wave capture factor:

$$\eta = \frac{2kP}{\rho g A^2 c_g} = \frac{khg}{c_g \sqrt{g/h}} \left\| \bar{\mathbf{C}}_{\text{PTO}}^{1/2} \left[-i(\bar{\mathbf{M}}_{\text{PTO}} + \bar{\mathbf{M}}) + (\bar{\mathbf{C}}_{\text{PTO}} + \bar{\mathbf{C}}) \right]^{-1} \bar{\mathbf{Q}}_e \right\|^2, \quad (4.4)$$

288 where the overbar indicates that the corresponding matrix is written in non-dimensional
289 format.

290 The rest of this paper focuses on the particular case in which all the OWCs have
291 the same size and the spacing between adjacent OWCs is constant, unless otherwise
292 specified. Moreover, all the OWCs are assumed to employ the same PTO system. Hence,
293 for the sake of convenience, $R_n = R$, $R_{i,n} = R_i$, $d_n = d$, $D_n = D$, $c_{\text{PTO},n} = c_{\text{PTO}}$ and
294 $a_{\text{PTO},n} = a_{\text{PTO}}$ are adopted, with which equation (4.4) simplifies to

$$\eta = \frac{khg\bar{c}_{\text{PTO}}}{c_g \sqrt{g/h}} \left\| \left[-i(\bar{a}_{\text{PTO}}\mathbf{I} + \bar{\mathbf{M}}) + (\bar{c}_{\text{PTO}}\mathbf{I} + \bar{\mathbf{C}}) \right]^{-1} \bar{\mathbf{Q}}_e \right\|^2, \quad (4.5)$$

295 where \mathbf{I} represents the square identity matrix of size $N \times N$. The chamber size and
296 chamber geometry of each OWC are fixed and cannot be easily adjusted. Following
297 Lovas *et al.* (2010); Martins-Rivas & Mei (2009*a,b*), here the value of a_{PTO} is calculated
298 based on $\rho/\rho_0 = 1000$, $v = 340$ m/s, $h = 10$ m and $V_0 = \pi R^2 h$, as $a_{\text{PTO}} = \omega V_0 / (v^2 \rho_0)$.
299 As a comparison, it might be more feasible to vary the value of c_{PTO} , e.g., to use several
300 turbines and control the blade angle and rotation speed, to strive for high efficiency for a
301 wide range of wave frequencies. In this paper, the corresponding optimal PTO damping
302 is considered equal to the optimum coefficient of the same coast-integrated OWC when
303 working in isolation (Lovas *et al.* 2010; Martins-Rivas & Mei 2009*a,b*). The wave power
304 capture factor contributed by the n -th OWC is denoted by η_n .

305 Apart from the wave power capture factor η , a q -factor is adopted as well to evaluate
306 the effect of the hydrodynamic interaction between the OWCs on power extraction:

$$q = \frac{\eta}{N\eta_0}, \quad (4.6)$$

307 where η_0 represents the maximum wave capture factor of an isolated coast-integrated
308 OWC. If $q > 1$, using an array of OWCs along the coast plays a constructive role in
309 power absorption. Whereas if $q < 1$, a destructive effect is induced by the hydrodynamic
310 interaction between the multiple coast-integrated OWCs.

311 In a similar way, the influence of the coast, i.e., the reflection effect, may be evaluated
312 by

$$q_c = \frac{\eta}{\eta'}, \quad (4.7)$$

313 in which η' denotes the wave capture factor of the corresponding offshore OWCs.

314 As given in equations (4.6) and (4.7), the subscript 0 and the superscript prime
315 represent the individual single isolated situation and the offshore situation, respectively.
316 Hence, $q' = \eta' / (N\eta'_0)$ can be used as the array factor to denote the constructive or
317 destructive hydrodynamic interaction between an array of offshore OWCs on power
318 extraction, in which η'_0 is the power capture factor of a single offshore OWC. Similarly,
319 $q_{c,0} = \eta_0 / \eta'_0$ can be used to calculate the reflection effect of the coast on a single coast-
320 integrated OWC.

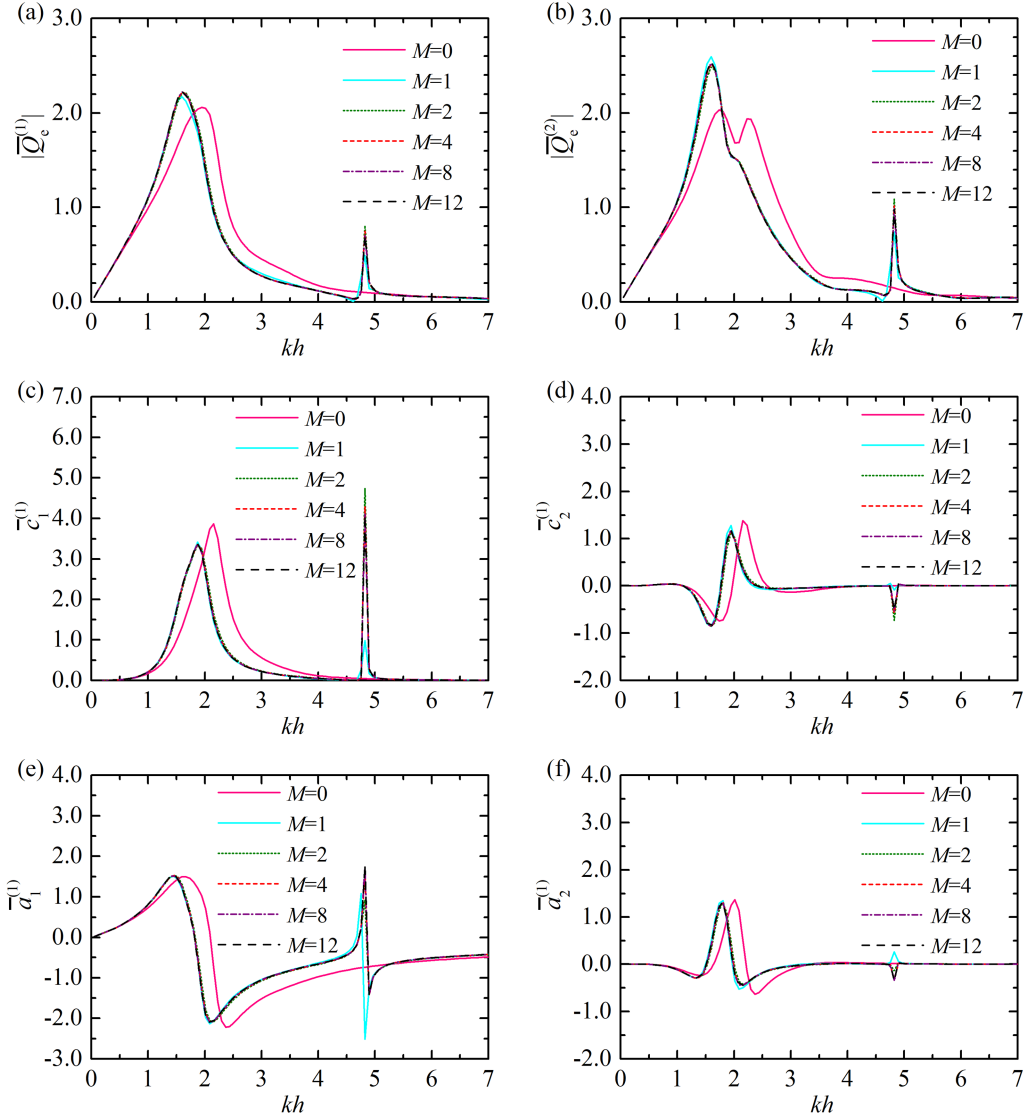


FIGURE 2. Impact of the angular cut-offs (i.e., in terms of M) on wave excitation volume flux and hydrodynamic coefficients, $N = 2$, $R/h = 0.5$, $(R - R_i)/h = 0.1$, $d/h = 0.2$, $D/h = 2.0$, $\beta = \pi/6$, $L = 20$: (a) $|\bar{Q}_e^{(1)}|$; (b) $|\bar{Q}_e^{(2)}|$; (c) $\bar{c}_1^{(1)}$; (d) $\bar{c}_2^{(1)}$; (e) $\bar{a}_1^{(1)}$; (f) $\bar{a}_2^{(1)}$.

5. Results and discussion

Figures 2 and 3 illustrate the impact of the angular and vertical truncated cutoffs (i.e., in terms of M and L), respectively, on the wave excitation volume flux and hydrodynamic coefficients for two coast-integrated OWCs with $R/h = 0.5$, $(R - R_i)/h = 0.1$, $d/h = 0.2$, $D/h = 2.0$ and $\beta = \pi/6$. Similarly, the convergence analysis was carried out for cases with a different number of OWCs and with different OWC geometry. In order to obtain the converged results, $M \geq 8$ and $L \geq 15$ are suggested. Hereinafter, $M = 12$ and $L = 20$ are adopted.

The present theoretical model is focused on an array of coast-integrated OWCs (i.e.,

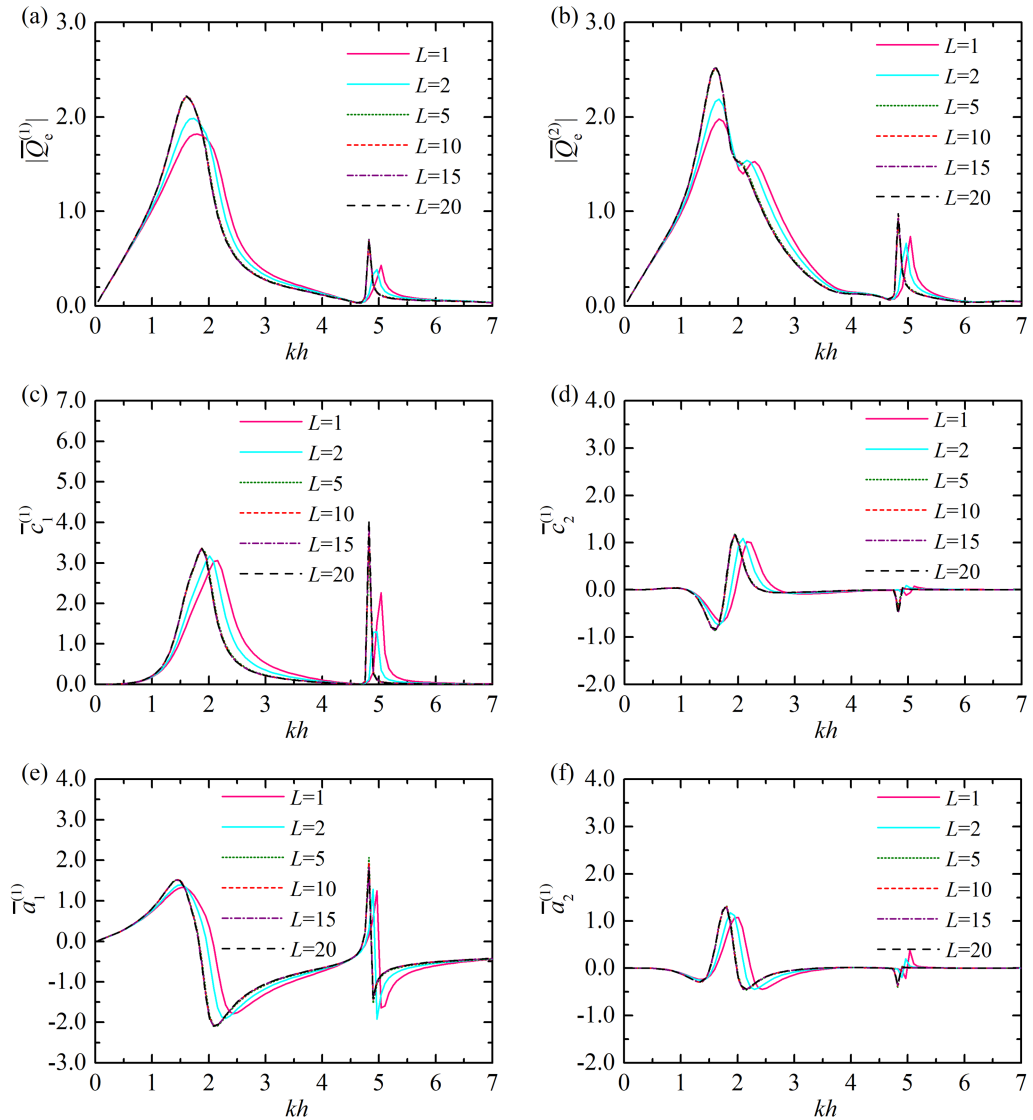


FIGURE 3. Impact of the vertical cut-offs (i.e., in terms of L) on wave excitation volume flux and hydrodynamic coefficients, $N = 2$, $R/h = 0.5$, $(R - R_i)/h = 0.1$, $d/h = 0.2$, $D/h = 2.0$, $\beta = \pi/6$, $M = 12$: (a) $|\bar{Q}_e^{(1)}|$; (b) $|\bar{Q}_e^{(2)}|$; (c) $\bar{c}_1^{(1)}$; (d) $\bar{c}_2^{(1)}$; (e) $\bar{a}_1^{(1)}$; (f) $\bar{a}_2^{(1)}$.

330 $N \geq 2$) without the thin-walled assumption (i.e., $R_i < R$). By contrast, if the OWCs are
 331 deployed far away from each other and the thickness of the OWC wall tends to zero (i.e.,
 332 $R_i \approx R$), the present model could be used to solve the hydrodynamic problems from a
 333 thin-walled coast-integrated OWC (i.e., $R_i = R$) approximately, which was investigated
 334 by Martins-Rivas & Mei (2009a). Figure 4 plots the frequency response of $c_1^{(1)}$ and $a_1^{(1)}$
 335 of the coast-integrated OWC(s) with $R/h = 0.5$ and $d/h = 0.2$. The present results with
 336 $N = 2$, $R_i/h = 0.49$, i.e., $(R - R_i)/R = 0.02$, and $D/h = 200$ are in good agreement with
 337 those of a single coast-integrated OWC under the thin-wall restriction (Martins-Rivas &
 338 Mei 2009a).

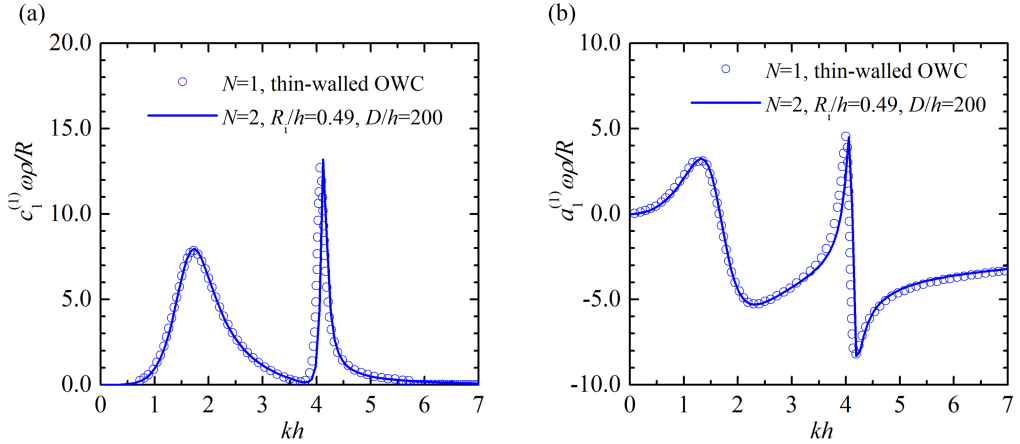


FIGURE 4. Frequency response of $c_1^{(1)}$ and $a_1^{(1)}$ of the coast-integrated OWC(s) with $R/h = 0.5$, $d/h = 0.2$: (a) $c_1^{(1)}$; (b) $a_1^{(1)}$. Circles: results from Martins-Rivas & Mei (2009a) for a thin-walled OWC, i.e., $R_i = R$; lines: present results for two OWCs far away from each other.

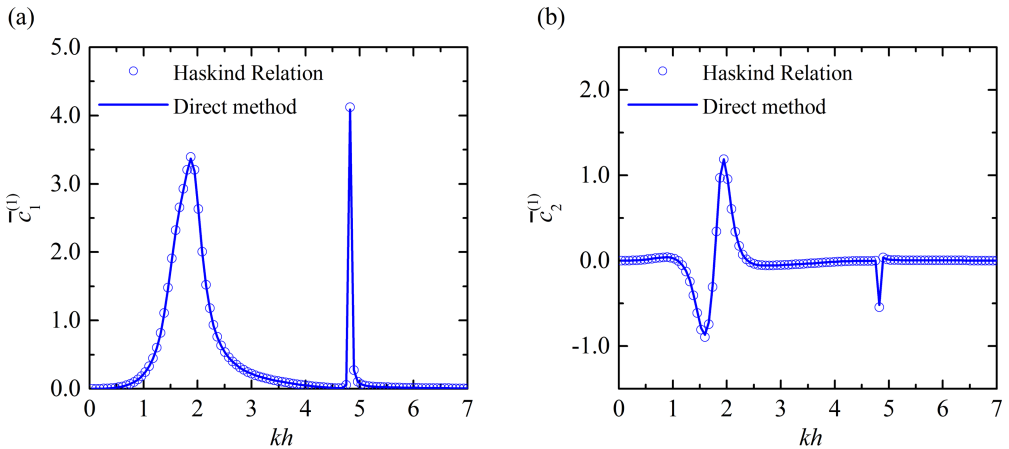


FIGURE 5. Results of wave damping coefficients by using the direct method and the indirect method based on the Haskind Relation, $N = 2$, $R/h = 0.5$, $(R - R_i)/h = 0.1$, $d/h = 0.2$, $D/h = 2.0$: (a) $\bar{c}_1^{(1)}$; (b) $\bar{c}_2^{(1)}$.

339 Additionally, figure 5 illustrates the behaviour of $\bar{c}_1^{(1)}$ and $\bar{c}_2^{(1)}$ versus the non-
 340 dimensional wavenumber kh for two coast-integrated OWCs with $R/h = 0.5$,
 341 $(R - R_i)/h = 0.1$, $d/h = 0.2$ and $D/h = 2.0$. The plotted results of $\bar{c}_1^{(1)}$ and $\bar{c}_2^{(1)}$
 342 obtained using the direct method and the Haskind relation cannot be distinguished.
 343 This excellent agreement between them, together with the results in figure 4, indicate
 344 the accuracy of separate computations of scattering and radiation potentials.

345 As displayed in figure 5a, there are two peaks of $\bar{c}_1^{(1)}$ ($kh = 1.88$ and 4.82) in the
 346 computed range of kh . Figure 6 presents the free-surface patterns ($\text{Re}(\xi_1 e^{-i\omega t})/A =$
 347 $\text{Re}(i\omega p_1 \Phi_1 e^{-i\omega t}/g)/A$) in- and outside the two OWC chambers corresponding to these
 348 two peaks of $\bar{c}_1^{(1)}$. Owing to the existence of the coast, the opening of each coast-integrated
 349 OWC is asymmetrical; as a result, in addition to the Helmholtz mode (the so-called
 350 pumping mode), another mode (i.e., the so-called sloshing mode) of the OWC is excited.

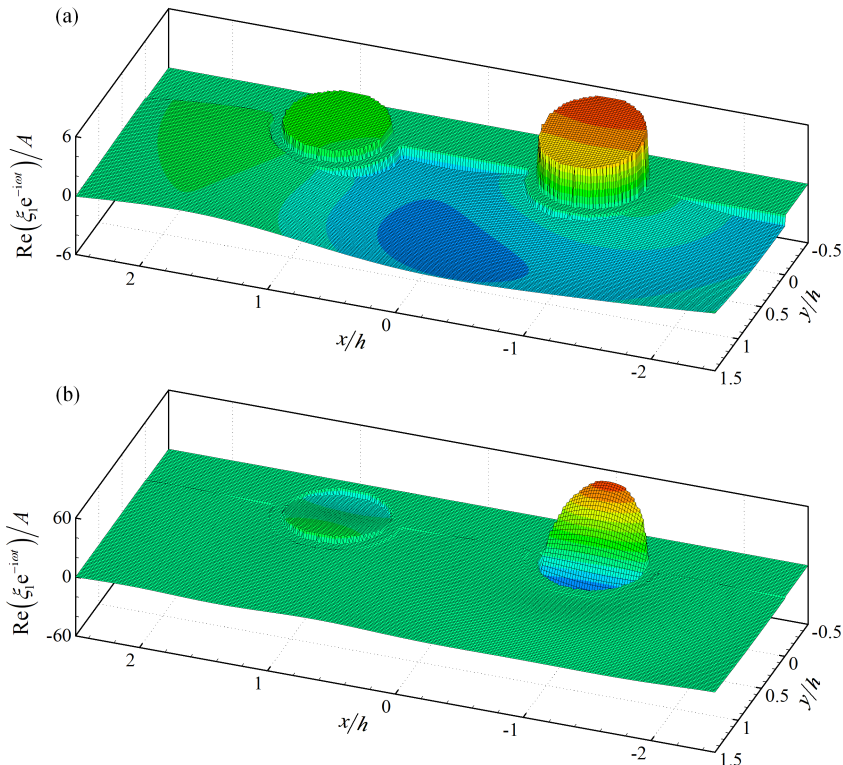


FIGURE 6. Radiation problem-free surface elevation inside and around the coast-integrated OWCs, $N = 2$, $R/h = 0.5$, $(R - R_i)/h = 0.1$, $d/h = 0.2$, $D/h = 2.0$, $p_1 = \rho g A$, $p_2 = 0$: (a) $kh = 1.88$ at $t = 3\pi/2\omega$; (b) $kh = 4.82$, at $t = \pi/2\omega$.

351 As shown in figure 6a, the pumping mode dominates the wave motion inside each OWC
 352 chamber for $kh = 1.88$. For $kh = 4.82$, as can be seen from figure 6b, the wave motion
 353 inside the OWC chambers is dominated by the sloshing mode.

354 As illustrated in figure 5, compared to the lower peak of $\bar{c}_1^{(1)}$ ($kh = 1.88$), the higher
 355 one ($kh = 4.82$) is sharper and much narrower. Here, as given in figure 7, $kh = 1.88$
 356 is taken as an example to present the scattering results of the free-surface patterns
 357 $(\text{Re}(\xi_0 e^{-i\omega t})/A = \text{Re}(i\omega\Phi_0 e^{-i\omega t}/g)/A)$ in- and outside the OWC chambers under incident
 358 waves with different angles of incidence: $\beta = \pi/6, \pi/4, \pi/3$ and $\pi/2$. Despite the fact that,
 359 generally speaking, the scattering wave motion around the integrated OWCs depends
 360 on the incident wave direction, the motion inside the OWC chambers is dominated by
 361 the pumping mode for $kh = 1.88$, regardless of the incident wave direction (figure 7).
 362 Although the sloshing mode plays a rather weak role for such a wave condition, it can
 363 still be observed from figure 7 that the symmetrical axis of that mode tends to align
 364 itself with the incident wave direction. For $\beta = \pi/2$, as expected, the two water columns
 365 behave the same due to the symmetry of both OWC geometry and wave field.

366 5.1. Comparison between multiple and single coast-integrated/offshore OWCs

367 Figure 8 displays the frequency responses of the hydrodynamic coefficients for
 368 two coast-integrated OWCs, the same OWCs in the open sea and a single coast-
 369 integrated/offshore OWC (Zheng *et al.* 2018, 2019). For all four cases in the full range
 370 of kh , $\bar{c}_1^{(1)}$ is positive (figure 8a), which is reasonable from the perspective of energy

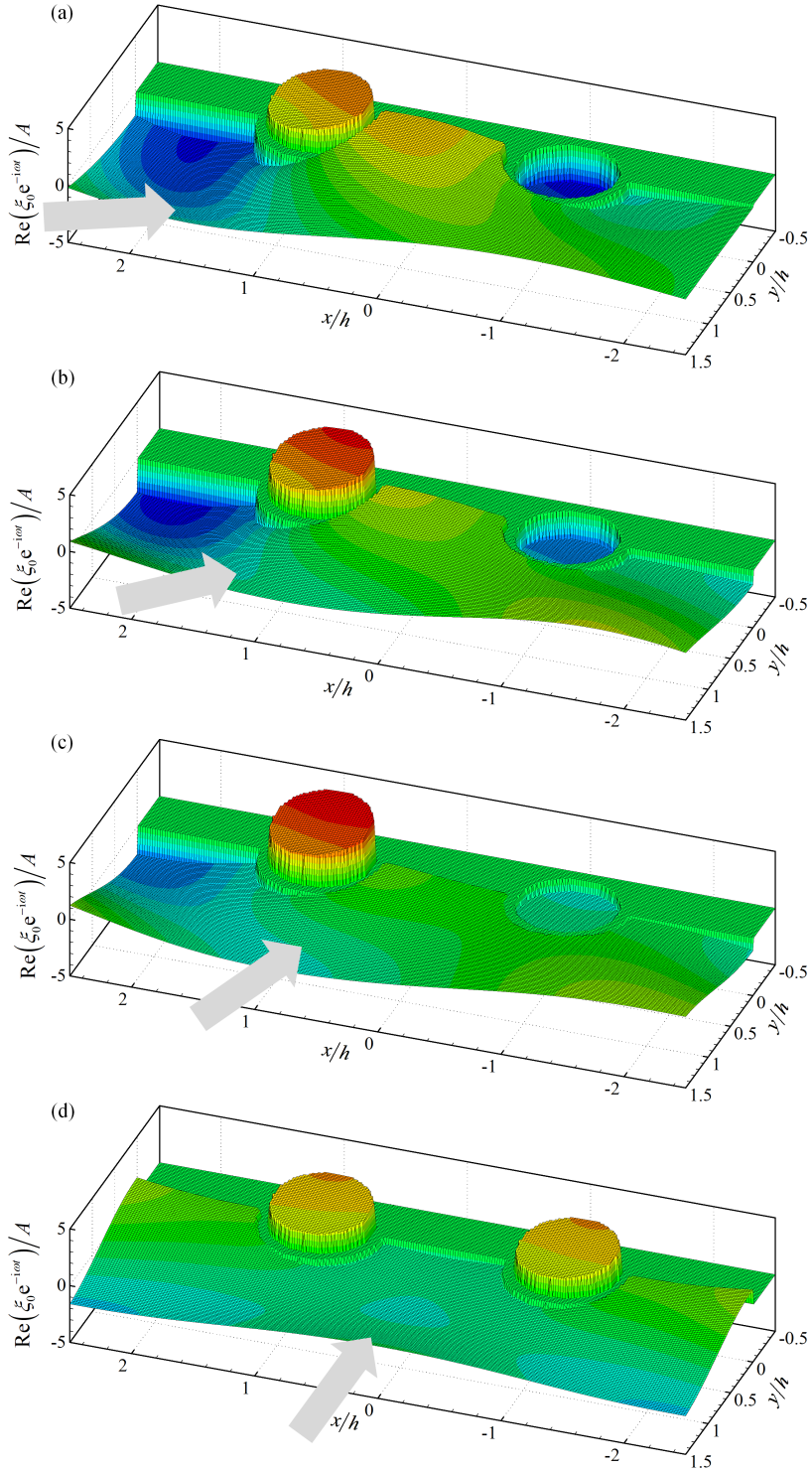


FIGURE 7. Scattering problem-free surface elevation inside and around the coast-integrated OWCs, $N = 2$, $R/h = 0.5$, $(R - R_i)/h = 0.1$, $d/h = 0.2$, $D/h = 2.0$, $t = 0$, $kh = 1.88$: (a) $\beta = \pi/6$; (b) $\beta = \pi/4$; (c) $\beta = \pi/3$; (d) $\beta = \pi/2$.

371 conservation and outgoing propagation of radiated waves (Zheng & Zhang 2018). For
 372 both the single and two offshore OWC(s) cases, there is only one peak of the $\bar{c}_1^{(1)}-kh$
 373 curve at $kh = 2.44$ in the computed range of kh , which corresponds to a pumping
 374 mode. The peak value of $\bar{c}_1^{(1)}$ for the two offshore OWCs is somewhat larger than that
 375 of the single offshore OWC due to the hydrodynamic interaction between them. For the
 376 single/two coast-integrated OWC(s) cases, two modes are excited - the lower (around
 377 $kh = 1.85$) dominated by the pumping mode, the higher (at $kh = 4.82$) dominated by
 378 the sloshing mode. Owing to the constraint of the coastline, the wave motion inside
 379 the OWC chamber is more restricted compared to that of the offshore cases, leading to
 380 smaller peaks of $\bar{c}_1^{(1)}$. As can be seen from figure 8c, the corresponding $\bar{a}_1^{(1)}$ parameter
 381 changes its sign rapidly around those kh values where the peaks of $\bar{c}_1^{(1)}$ occur. Since
 382 the effect of hydrostatic stiffness has already been included in $\bar{a}_1^{(1)}$, the kh values where
 383 $\bar{a}_1^{(1)}$ vanishes correspond to natural resonance. The light grey line plotted in figure 8c
 384 represents $-\bar{a}_{PTO}$, which is induced by the air compressibility. When taken into account,
 385 resonance happens at the kh values where the $\bar{a}_1^{(1)}$ and $-\bar{a}_{PTO}$ curves intersect each
 386 other. For the two offshore/coast-integrated OWCs (figures 8b and 8d), the ranges of
 387 $\bar{c}_2^{(1)}$ and $\bar{a}_2^{(1)}$ are comparable to those of $\bar{c}_1^{(1)}$ and $\bar{a}_1^{(1)}$, indicating the significant influence
 388 of the hydrodynamic interaction between multiple OWCs.

389 The frequency responses of the wave excitation volume flux in terms of the amplitude
 390 and phase for these four cases subjected to incident waves with $\beta = \pi/2$ are plotted
 391 in figure 9. The basic shapes of the $|\bar{Q}_e^{(1)}|-kh$ curves (figure 9a) look similar to those
 392 of $\bar{c}_1^{(1)}-kh$ (figure 8a). However, due to the wave reflection from the vertical coastline,
 393 the peaks of $|\bar{Q}_e^{(1)}|$ for the coast-integrated OWC(s) are larger than those of offshore
 394 situations, and clearly shift towards lower frequencies. The shift of the position of the
 395 peaks can be explained from the point of view of the natural modes: compared to the
 396 offshore OWC(s), for which the space under the chamber wall is entirely open to the
 397 water, in the case of the coast-integrated OWC(s), half of the space below the chamber
 398 on the coast side is closed, implying that a greater proportion of the water column is
 399 enclosed. This leads to smaller natural frequencies and, therefore, the OWC(s) are more
 400 likely to be significantly excited at lower frequencies. The peaks of $|\bar{Q}_e^{(1)}|$ for the two
 401 OWCs, regardless of whether they are coast-integrated or offshore, can benefit from the
 402 hydrodynamic interaction between them, e.g., the peak value of $|\bar{Q}_e^{(1)}|$ of 2.69 for the
 403 single coast-integrated OWC, which is reached for $kh = 1.73$, is enhanced to 3.64 for
 404 the two coast-integrated OWCs, and occurs at $kh = 1.88$. In long waves, e.g., $kh < 1.5$,
 405 the size of the OWCs is small compared to the wavelength, so that the primary effect
 406 on the wave field is reflection at the coast, leading to an overlapping of $\varphi_e^{(1)}-kh$ for the
 407 single/two OWC(s) cases and a separation for offshore and coast-integrated situations
 408 (figure 9b).

409 The wave power extraction from these four cases of OWC(s) are displayed in figure 10
 410 in terms of power capture factor, array factor, coast factor and PTO damping employed.
 411 The curve of $-\bar{a}_{PTO}$ intersects the curve of $\bar{a}_1^{(1)}$ at two values of kh , i.e., 2.47 and 4.19,
 412 in the computed range of kh for single/two offshore OWC(s) (see figure 8c), and the
 413 corresponding wave capture factors (η' and η'_0) as shown in figure 10a also attain their
 414 optimum at these two wave frequencies. The value of η'_0 is exactly 1.0 at the resonant
 415 frequencies displayed, which is reasonable and can be theoretically derived by using
 416 the Haskind relation (e.g., Falnes (2002)). For the two offshore OWCs case, the largest
 417 value of the wave capture factor (η' as displayed in figure 10a) can reach 2.27. There

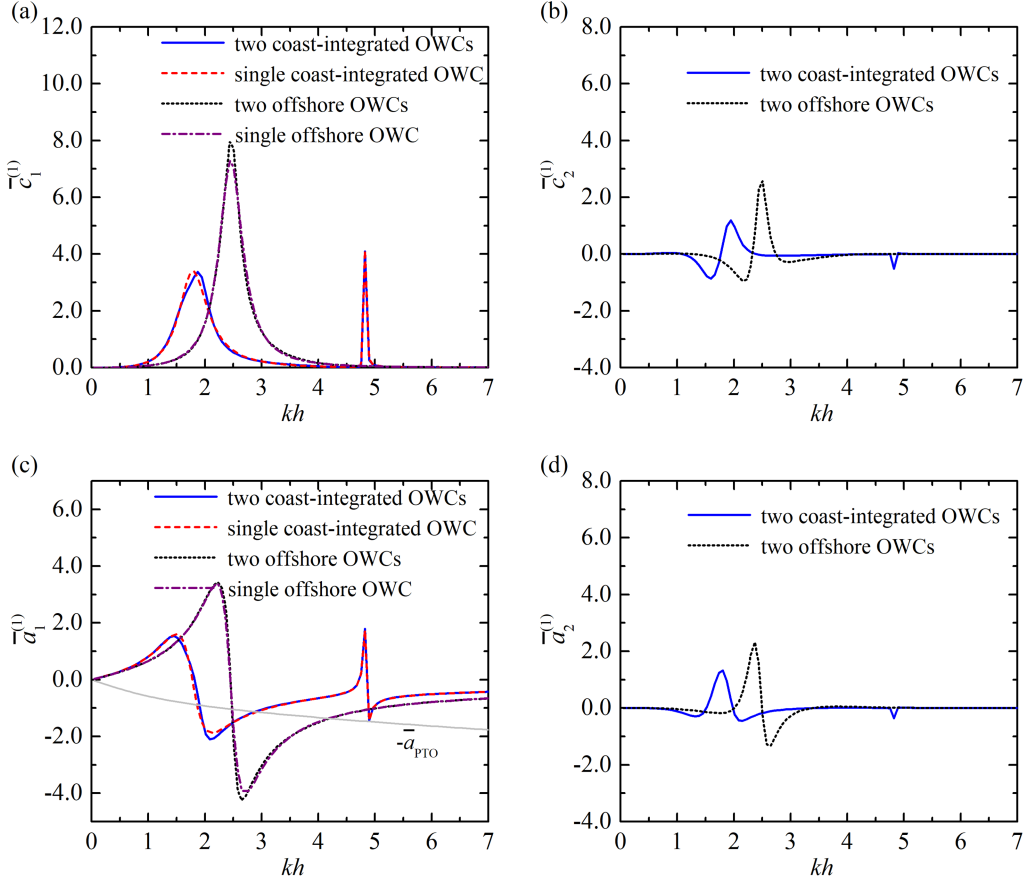


FIGURE 8. Radiation problem, $R/h = 0.5$, $(R - R_i)/h = 0.1$, $d/h = 0.2$, $D/h = 2.0$, $h = 10$ m: (a) $\bar{c}_1^{(1)}$; (b) $\bar{c}_2^{(1)}$; (c) $\bar{a}_1^{(1)}$ and $-\bar{a}_{PTO}$; (d) $\bar{a}_2^{(1)}$.

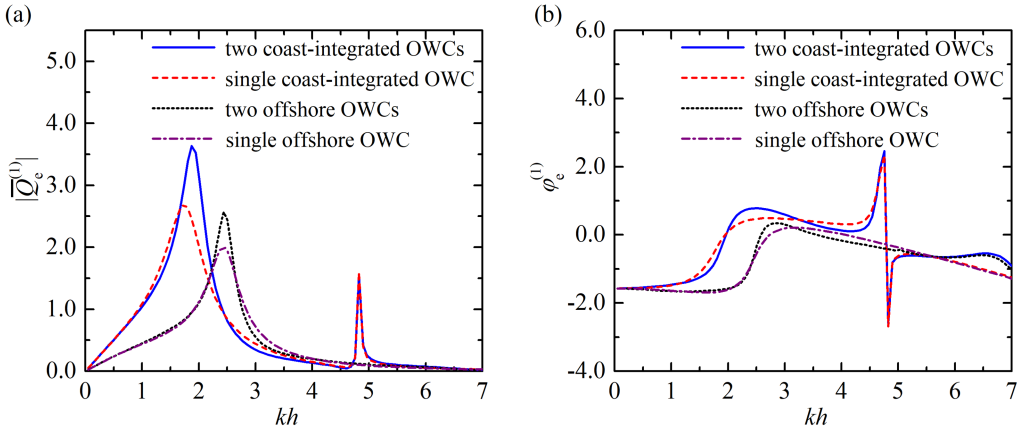


FIGURE 9. Scattering problem, $R/h = 0.5$, $(R - R_i)/h = 0.1$, $d/h = 0.2$, $D/h = 2.0$, $\beta = \pi/2$: (a) amplitude of wave excitation volume flux, $|\bar{Q}_e^{(1)}|$; (b) phase of wave excitation volume flux, $\varphi_e^{(1)}$.

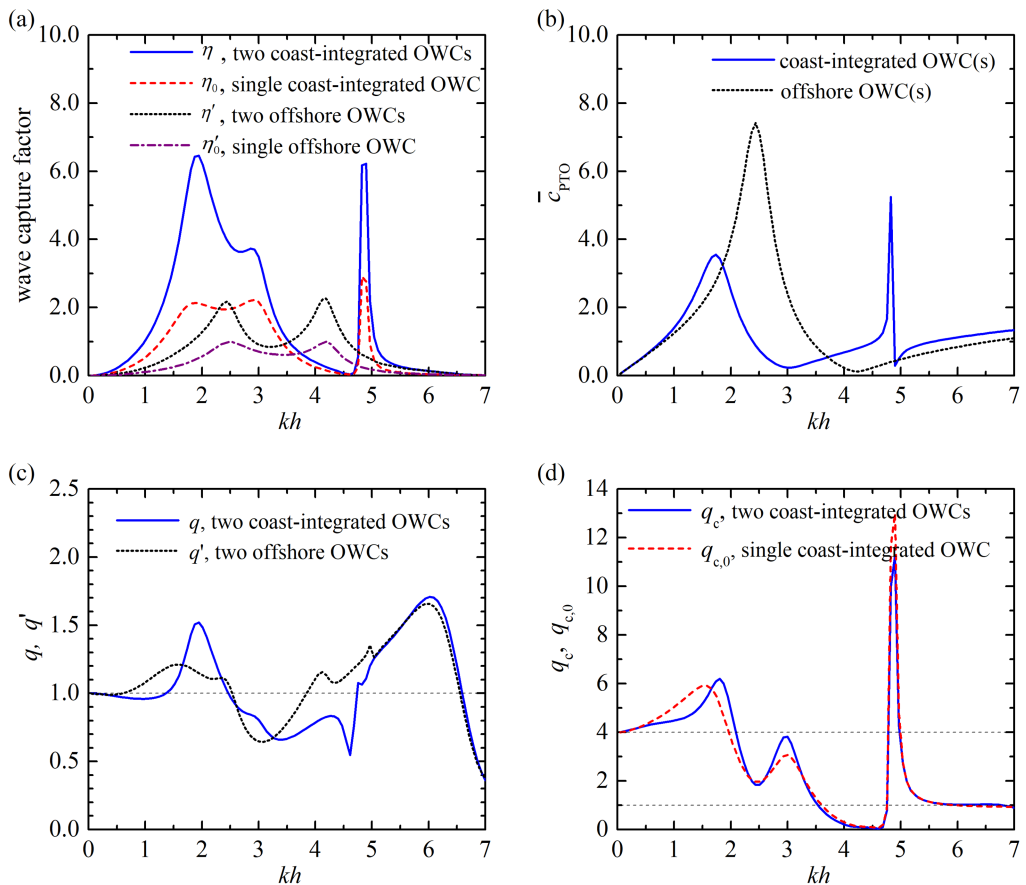


FIGURE 10. Power extraction, $R/h = 0.5$, $(R - R_i)/h = 0.1$, $d/h = 0.2$, $D/h = 2.0$, $\beta = \pi/2$, $h = 10$ m: (a) wave capture factor, η , η_0 , η' and η'_0 ; (b) \bar{c}_{PTO} ; (c) array factor, q and q' ; (d) coast factor, q_c and $q_{c,0}$.

418 is an obvious drop in η' between these two resonant frequencies, for $kh \in (3.0, 3.5)$,
 419 implying that the two OWCs cannot continuously capture wave power effectively in a
 420 large range of kh . When the OWC(s) is(are) integrated into a coast, three intersections
 421 of $\bar{a}_1^{(1)}$ and $-\bar{a}_{\text{PTO}}$ occur, at $kh = 1.88, 2.92$ and 4.82 (figure 8c), resulting in three
 422 peaks of η and η_0 (figure 10a). Compared to those of the offshore cases, although the
 423 first two resonant frequencies of the coast-integrated cases are closer to each other, η_0
 424 remains mostly around 2.0 for kh between these two frequencies, leading to an even
 425 broader bandwidth of high efficiency. For the two coast-integrated OWCs, thanks to the
 426 constructive hydrodynamic interaction between them, a large peak value of η , 6.46, is
 427 achieved around $kh = 1.88$. The corresponding \bar{c}_{PTO} (figure 10b) shows that, in order
 428 to reach optimum efficiency for all wave conditions, the turbine parameter for the coast-
 429 integrated cases does not need to be varied as much as that in the offshore cases, making
 430 it relatively easy to achieve in practice.

431 The variation of the array factor for the coast-integrated and offshore cases (i.e., q and
 432 q') with kh (figure 10c) indicates that both q and q' tend to unity as kh tends to 0. As a
 433 comparison, the coast reflection effect factor for single/two coast-integrated cases (i.e., q_c
 434 and $q_{c,0}$, figure 10d) tends to 4.0 when kh tends to 0. This is due to the fact that incident

435 waves are the dominant element in the excitation volume flux under long waves. In the
 436 open sea, the amplitude of undisturbed incident waves is A , whereas the amplitude of
 437 incident waves subjected to reflection from the vertical coast turns out to be $2A$, leading
 438 to a doubling of the excitation volume flux and, in turn, affecting wave power extraction.
 439 For short waves, e.g., $kh > 5.5$, the curves of q and q' tend to overlap each other and
 440 the values of q_c and $q_{c,0}$ both approach unity. This can be explained by the dominant
 441 role of \bar{c}_{PTO} and \bar{a}_{PTO} in the wave power capture factor (refer to equation (4.5)) in short
 442 wave conditions. For $kh > 6.0$, all hydrodynamic coefficients vanish alongside the wave
 443 excitation volume flux (figures 8-10), whereas \bar{c}_{PTO} and \bar{a}_{PTO} remain non-vanishing and
 444 become even larger with the increase of kh . As displayed in figure 10d, for most wave
 445 conditions, except $kh \in (3.5, 4.8)$ and $kh > 5.5$, the coast factors remain far above unity,
 446 indicating a constructive effect of coast reflection on wave power absorption. However,
 447 the array factor oscillates around 1.0 and shows alternating constructive and destructive
 448 effects with the change of kh (figure 10c). In the following sections, only the wave capture
 449 factor and array factor are preserved to indicate power extraction of the coast-integrated
 450 OWCs. As can be seen from figures 10a, 10c and 10d, the dramatic peak of η occurring at
 451 $kh = 1.88$ benefits from both the constructive array effect ($q = 1.5$) and the constructive
 452 coast effect ($q_c = 6.0$).

5.2. Effect of incident wave direction

453
 454 The wave excitation volume flux of each OWC, the power capture factor of each OWC
 455 and both together with the q -factor for different incident wave directions β are displayed
 456 in figure 11. As β increases from $\pi/6$ to $\pi/2$, the main peak of the wave excitation volume
 457 flux of the up-wave OWC ($|\bar{Q}_e^{(2)}|$) becomes larger and shifts towards large kh . The first
 458 peak for the other OWC ($|\bar{Q}_e^{(1)}|$), on the contrary, first falls and shifts towards small
 459 kh , and then rises and shifts in the opposite direction rapidly to the same position of
 460 $|\bar{Q}_e^{(2)}|$ for $\beta = \pi/2$. Note that, at $kh \approx 2.0$, a slight rise of the $|\bar{Q}_e^{(1)}|$ or $|\bar{Q}_e^{(2)}|$ curves
 461 with specified values of β is observed, e.g., more particularly, an additional peak of the
 462 $|\bar{Q}_e^{(1)}|$ - kh curve for $\beta = \pi/3$ can be excited. This appears to be induced by the resonance
 463 of water waves between the two OWCs, for $k(D - R) \approx \pi$ is satisfied for these cases at
 464 $kh \approx 2.0$. For $\beta = \pi/6$ and $\pi/4$, the wave power capture factor of the up-wave OWC
 465 (η_2) is generally larger than the down-wave one (η_1) for $kh \in (1.5, 3.5)$ (figure 11b),
 466 whereas for $\beta = \pi/3$, $\eta_1 > \eta_2$ is observed for $kh \in (2.0, 3.0)$. As displayed in figure
 467 11c, for $kh \in (1.5, 2.0)$, the overall power capture factor (η) increases dramatically with
 468 the increase of β from $\pi/6$ to $\pi/2$. For $kh \in (2.6, 4.0)$, the η corresponding to $\beta = \pi/3$
 469 is significantly greater than those for all three other incident wave directions, including
 470 $\beta = \pi/2$. This can be explained from the perspective of the array effect as illustrated in
 471 figure 11d, in which constructive ($q > 1.0$) and destructive ($q < 1.0$) effects are indicated
 472 for $\beta = \pi/3$ and $\pi/2$, respectively, for $kh \in (2.6, 4.0)$. The following sections focus on the
 473 cases with $\beta = \pi/2$.

474 Note that, at $kh = 1.88$, the maximum η for $\beta = \pi/2$ is dramatically higher than 4.0,
 475 while the η values for $\beta = \pi/6$ and $\pi/4$ are obviously lower than 4.0. Instead, at $kh = 2.92$,
 476 the η values for the four cases with different values of β are all concentrated around 4.0.
 477 In fact, for any certain wave frequency, there is a general identity of the optimum wave
 478 capture factor (η_{MAX}) over all incidence angles that multiple coast-integrated OWCs
 479 must hold regardless of the OWC dimension, i.e.,

$$\frac{1}{\pi} \int_0^\pi \eta_{\text{MAX}}(\beta) d\beta = 2N, \quad (5.1)$$

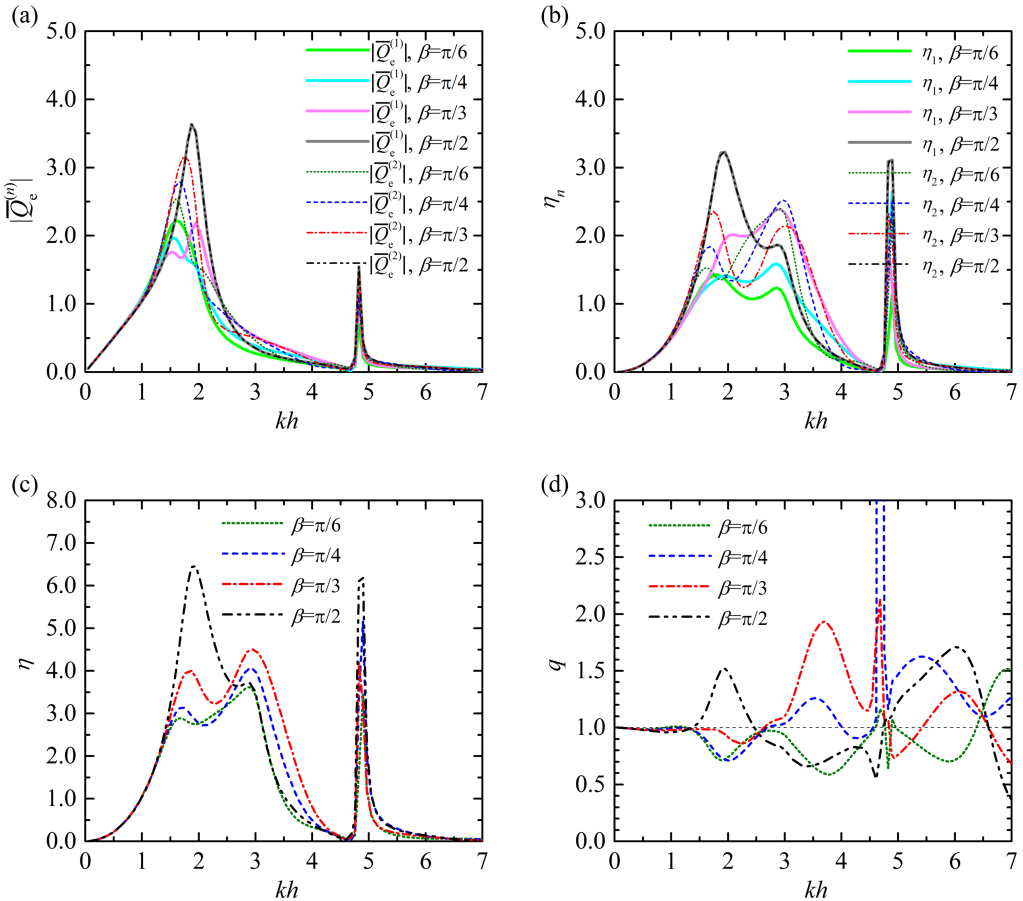


FIGURE 11. Comparison for different incident direction, β , with $N = 2$, $R/h = 0.5$, $(R - R_i)/h = 0.1$, $d/h = 0.2$, $D/h = 2.0$, $h = 10$ m: (a) $|\bar{Q}_e^{(n)}|$; (b) η_n ; (c) η ; (d) q -factor.

480 which can be theoretically confirmed by invoking the ideal optimization criteria and the
 481 Haskind relation (Wolgamot *et al.* 2012). A detailed derivation is given in Appendix B.

482

5.3. Effect of radius of the OWCs

483

484

485

486

487

488

489

490

491

492

493

494

495

The effect of radius (R/h) of the OWCs on wave excitation volume flux, hydrodynamic coefficients, wave capture factor and array factor were investigated (figure 12). As R/h increases from 0.3 to 0.7, the main peak of the $|\bar{Q}_e^{(n)}|$ curve, as shown in figure 12a, shifts towards lower frequencies and tends to be flatter. The peak value first becomes larger and then smaller after reaching the largest value with $R/h = 0.5$. As illustrated in figure 12b, for the smallest column $R/h = 0.3$, the curve of $\bar{c}_1^{(1)}$ has only one peak in the computed range of kh . For larger R/h , i.e., $R/h = 0.4 \sim 0.6$ and $R/h = 0.7$, two and three peaks, are evident, respectively. This is associated with the natural resonance modes (without PTO system), which are strongly dependent on the relative size of OWC chamber to wavelength. Figure 12(c,e) indicates that, with the increase of R/h , the oscillation amplitudes of the $\bar{c}_2^{(1)}$ and $\bar{a}_2^{(1)}$ curves become larger, and the kh corresponding to these largest amplitudes get smaller. As previously defined in Section 4, \bar{a}_{PTO} depends on the chamber volume $V_0 = \pi R^2 h$, which in turn depends critically on R/h .

496 In figure 12d, apart from the five curves of $\bar{a}_1^{(1)}$, five solid thin curves of $-\bar{a}_{\text{PTO}}$
 497 relating to five different values of R/h are plotted in the corresponding colour. For
 498 $R/h = 0.3$, there are two points of interaction between $-\bar{a}_{\text{PTO}}$ and $\bar{a}_1^{(1)}$ in the range
 499 of kh plotted; while for larger R/h , more points of interaction can be achieved, e.g., four
 500 interaction points for $R/h = 0.7$. As R/h increases from 0.3 to 0.7, the curve of $-\bar{a}_{\text{PTO}}$ is
 501 slanted downwards, resulting in the first two points of interaction moving towards lower
 502 frequencies and the horizontal distance between them getting smaller. The kh values
 503 corresponding to the points of interaction between $-\bar{a}_{\text{PTO}}$ and $\bar{a}_1^{(1)}$ identified from figure
 504 12d coincide well with the peak positions of the η curves (figure 12f). As R/h increases,
 505 the main peaks of the η curve shift towards lower kh and gain intensity. Figure 12g shows
 506 that the q -factor remains above unity for $kh \in (1.4, 2.5)$ regardless of the value of R/h .
 507 For $R/h = 0.7$, constructive array effects can be obtained for a rather large range of kh ,
 508 i.e., $kh \in (1.4, 3.3)$. Although some higher and broader peaks of q can be achieved for
 509 $kh > 4.5$, they are not attractive, because either η is too small, or η is only large in a
 510 narrow bandwidth.

511 5.4. Effect of wall thickness of the OWCs

512 The theoretical results for the OWCs with different chamber wall thickness are plotted
 513 in figure 13. As the wall thickness of the OWC chambers increases, i.e., the inner radius
 514 of the chamber decreases while the outer radius remains constant, the main peak of $|\bar{Q}_e^{(n)}|$
 515 shifts slightly towards higher wave frequencies with a narrower bandwidth (figure 13a),
 516 while its peak height remains approximately the same. A similar change occurs for $\bar{c}_1^{(1)}$
 517 (figure 13b), with the main peak becoming higher and more abrupt with the increase
 518 of wall thickness of the OWCs. Correspondingly, the first sign changing point of $\bar{a}_1^{(1)}$
 519 (figure 13d) occurs at a lower frequency, and its variation in amplitude gets larger, and
 520 happens in a narrower range of kh . With the increase of wall thickness, the position of
 521 the largest oscillation amplitude of $\bar{c}_2^{(1)}$ and $\bar{a}_2^{(1)}$ (figure 13c,e) moves towards large kh
 522 and the variation becomes more abrupt as well. As illustrated in figure 13f, the peaks of
 523 η at $kh \in (1.0, 3.5)$ are lower and the overall bandwidth is narrower for a thicker wall of
 524 each OWC chamber. This can also be reflected by the intersections between the $-\bar{a}_{\text{PTO}}$
 525 and $\bar{a}_1^{(1)}$ curves (figure 13d), which get closer to each other horizontally. In figure 13g,
 526 a smaller q -factor is shown to be obtained for the OWCs with a thicker chamber wall
 527 for most $kh \in (1.8, 3.5)$, suggesting a relatively more destructive array effect. Hence it
 528 may be concluded that to achieve higher wave power absorption efficiency in a broader
 529 bandwidth, the OWC chambers with a thinner wall are more appropriate. It should
 530 be noted that in practice the chamber wall should not be so thin as to lose structural
 531 robustness.

532 5.5. Effect of submergence of the OWCs

533 The submergence of the chamber, d/h , can also strongly affect the hydrodynamics and
 534 power extraction of the coast-integrated OWCs. As indicated in figures 14b and 14d, the
 535 peaks of $\bar{c}_1^{(1)}$ and the sign changing points of $\bar{a}_1^{(1)}$ are found to shift towards lower kh with
 536 the increase of d/h . This is reasonable, since a larger d/h means a higher, heavier water
 537 column enclosed within the chamber, leading to a smaller natural frequency. As d/h
 538 increases, the curve of $|\bar{Q}_e^{(n)}|$ becomes more abrupt (figure 14a), and the peaks become
 539 higher and move towards low kh . As indicated in figures 14c and 14e, the frequencies
 540 corresponding to the dramatic variations of $\bar{c}_2^{(1)}$ and $\bar{a}_2^{(1)}$ decrease with increasing d/h . It
 541 is worth noting that, with the decrease of d/h , although the peaks of the η curve remain

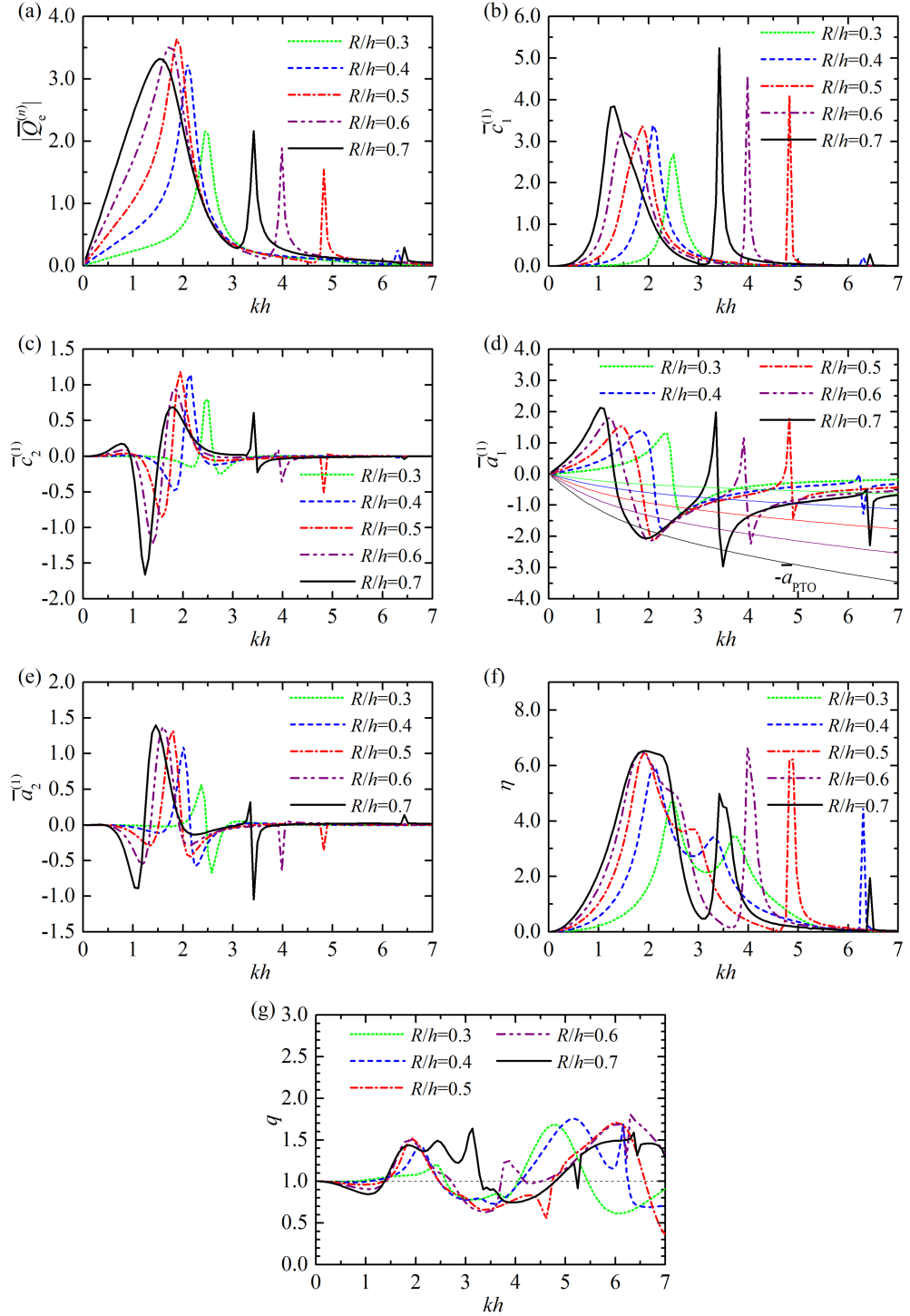


FIGURE 12. Comparison for different radius of the OWCs, R/h , with $N = 2$, $(R - R_i)/h = 0.1$, $d/h = 0.2$, $D/h = 2.0$, $\beta = \pi/2$, $h = 10$ m: (a) $|\bar{Q}_e^{(n)}|$; (b) $\bar{c}_1^{(1)}$; (c) $\bar{c}_2^{(1)}$; (d) $\bar{a}_1^{(1)}$ and $-\bar{a}_{PTO}$ (solid thin curves in the same colour of $\bar{a}_1^{(1)}$ for the same value of R/h); (e) $\bar{a}_2^{(1)}$; (f) η ; (g) q -factor.

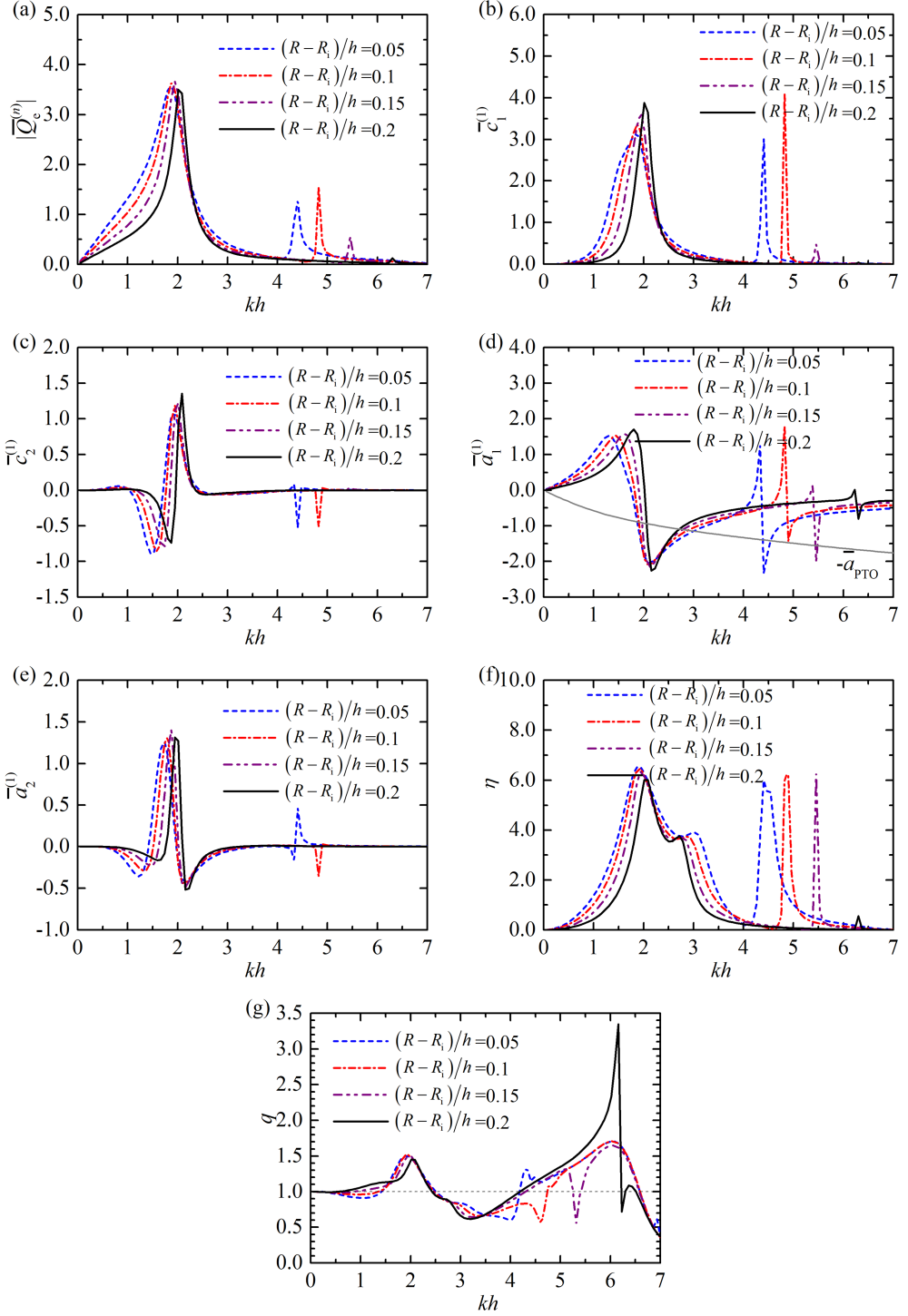


FIGURE 13. Comparison for different wall thickness of the OWCs, $(R - R_i)/h$, with $N = 2$, $R/h = 0.5$, $d/h = 0.2$, $D/h = 2.0$, $\beta = \pi/2$, $h = 10$ m: (a) $|\bar{Q}_e^{(n)}|$; (b) $\bar{c}_1^{(1)}$; (c) $\bar{c}_2^{(1)}$; (d) $\bar{a}_1^{(1)}$ and $-\bar{a}_{PTO}$; (e) $\bar{a}_2^{(1)}$; (f) η ; (g) q -factor.

at approximately the same levels (figure 14f), there is a distinct movement of these peaks towards large kh , which can be indicated as well from the position changes of the intersections between the $-\bar{a}_{\text{PTO}}$ and $\bar{a}_1^{(1)}$ curves (figure 14d). Furthermore, broader and smoother peaks of η are achieved for a smaller d/h as shown in figure 14f. For short waves, e.g., $kh \in (5.5, 7.0)$, more power can be captured with the decrease of d/h , and this constructive effect becomes stronger and stronger. This is due to the fact that most wave power (approximately 95%) is concentrated at no more than one-quarter of a wavelength below the still-water level, where the kinetic energy at a shallower position is more intensive compared to that at a deeper position. For most wave conditions at $kh \in (2.2, 3.6)$, a larger q -factor is obtained for a smaller d/h (figure 14g). Therefore, to have a better array effect and ultimately to achieve high power absorption in a rather broader bandwidth, the submergence of the OWC chambers should be as small as possible. However, the realistic chamber submergence cannot be too small, otherwise the opening may not be continuously submerged in the water when the OWCs are subjected to either strong waves or a large tidal range.

5.6. Effect of distance between the OWCs

Figure 15 presents the effect of distance between the OWCs. Similar results for the individually isolated single coast/breakwater-integrated OWC (denoted as “isolated”) are also displayed for comparison. Figure 15a shows that there are two peaks of the $|\bar{Q}_e^{(n)}|-kh$ curve over the computed range of kh , with the main one around $kh \approx 1.8$ and the second sharp one at a higher frequency, i.e., $kh \approx 4.82$. As D/h increases from 1.5 to 3.0, the amplitude of the main peak first increases and then decreases. Although the amplitude of the main peak for $D/h = 1.5$ is merely 2.4, large values of $|\bar{Q}_e^{(n)}|$ compared to the other cases are obtained at $kh \in (2.1, 3.0)$. The kh corresponding to the main peak shifts towards lower frequencies. The second sharp peak is nearly independent of D/h . As shown in figures 15b and 15d, a rather limited impact of D/h on $\bar{c}_1^{(1)}$ and $\bar{a}_1^{(1)}$ is observed at $kh \in (1.5, 2.5)$, where the main peak of the $\bar{c}_1^{(1)}-kh$ curve and the corresponding drop of $\bar{a}_1^{(1)}$ occur. As D/h varies, the $\bar{c}_1^{(1)}$ ($\bar{a}_1^{(1)}$)- kh curve of the two OWCs oscillates slightly around that of the “isolated” case. This is due to the fact that the waves radiated from each coast/breakwater-integrated OWC, and also those waves diffracted from the other OWC, act on the OWC in question simultaneously. The change in D/h leads to alteration of the phase difference between the two-OWCs mutual radiated and diffracted waves, resulting in the switch of reinforcing and diminishing influences. The amplitudes of the peak of $\bar{c}_1^{(1)}$ and the drop of $\bar{a}_1^{(1)}$ at $kh = 1.8$ are both approximately 3.5.

As a comparison (figures 15c and 15e), the variations of $\bar{c}_2^{(1)}$ and $\bar{a}_2^{(1)}$, especially for $kh \in (1.0, 3.0)$, are significantly dependent upon D/h . The amplitudes of the drops of $\bar{c}_2^{(1)}$ and $\bar{a}_2^{(1)}$ around $kh = 1.8$ are both found to be no smaller than 1.6, revealing a strong hydrodynamic interaction between the OWCs for the four cases of D/h examined. As D/h increases from 1.5 to 3.0, these drops of $\bar{c}_2^{(1)}$ and $\bar{a}_2^{(1)}$ become progressively weaker, and it can be expected that for $D/h \rightarrow \infty$, $\bar{c}_2^{(1)} \approx 0$ and $\bar{a}_2^{(1)} \approx 0$ will be obtained. The wave power capture factor of the “isolated” case, i.e., η_0 , is no more than 2.0 (figure 15f). However, for the cases consisting of two OWCs, the value of $\eta > 6.0$ can be obtained for certain values of D/h due to hydrodynamic interactions. From the perspective of the peak value of η , the OWCs with $D/h = 2.0$ could be the best solution for power absorption. However, in practice, the OWCs with $D/h = 1.5$ might be a better choice for their good performance over a broader bandwidth, with a sufficiently large wave capture factor. It can be learned (figure 15g) that, indeed, the D/h ratio has a strong effect on the

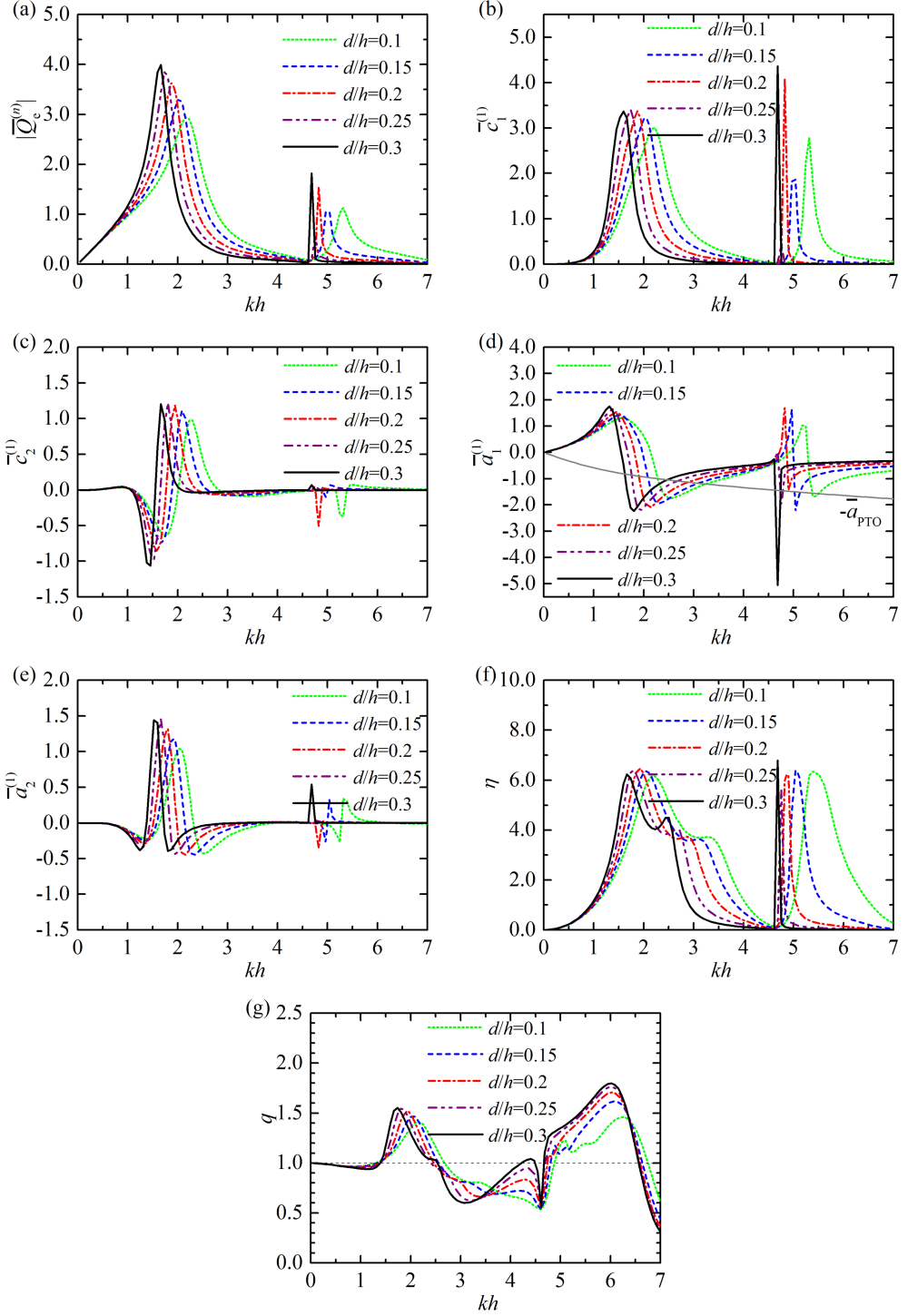


FIGURE 14. Comparison for different submergence of the OWCs, d/h , with $N = 2$, $R/h = 0.5$, $(R - R_i)/h = 0.1$, $D/h = 2.0$, $\beta = \pi/2$, $h = 10$ m: (a) $|\bar{Q}_e^{(n)}|$; (b) $\bar{c}_1^{(1)}$; (c) $\bar{c}_2^{(1)}$; (d) $\bar{a}_1^{(1)}$ and $-\bar{a}_{\text{PTO}}$; (e) $\bar{a}_2^{(1)}$; (f) η ; (g) q -factor.

589 shape of the q -factor curve as well as on its amplitude. For $D/h = 1.5$, $q > 1.0$ is satisfied
 590 at $kh \in (1.8, 3.4)$, meaning that a constructive hydrodynamic interaction between the
 591 OWCs is achieved in a large range of wave conditions.

5.7. Effect of the number of OWCs

592
 593 The frequency responses of the wave power capture factor of each OWC for $N = 2, 3, 4$
 594 and 5, together with the overall q -factor, are plotted in figure 16. The wave power capture
 595 factor of the isolated single coast/breakwater-integrated OWC (i.e., η_0) are also displayed
 596 as a comparison. Since the OWCs with the same size are uniformly distributed along the
 597 straight coast and are subjected to incident waves with $\beta = \pi/2$, the performance of an
 598 individual OWC is the same as the one symmetrical about the centrosymmetric plane
 599 of the OWC array. For the sake of simplicity, only the results of the first half number
 600 of OWCs are displayed, including the middle one as well if N is odd. It is shown in
 601 figures 16a - 16d that, from the perspective of the peak value of the power capture
 602 factor, the performance of each OWC among the multiple OWCs is better than that of
 603 the single isolated coast-integrated OWC. The closer the OWC is to the middle position
 604 of the array, the higher its peak power capture factor. For other wave conditions rather
 605 than the peak frequencies, e.g., $kh \in (2.8, 3.5)$, less power can be extracted by an OWC
 606 in an array of OWCs, compared to the single isolated coast-integrated case. Moreover,
 607 much less can be captured by the OWC closer to the middle position of the array. This
 608 tendency of the performances of an array of OWCs compared to a single OWC can also
 609 be clearly detected from the q -factor as plotted in figure 16e. For $kh \in (2.0, 2.5)$, although
 610 $q > 1$ is achieved for all the examples considered, the q value for two OWCs is obviously
 611 smaller than those with more OWCs. It might be concluded that for such a range of wave
 612 conditions, an array of coast-integrated OWCs consisting of three or more OWCs could
 613 be a better choice, to benefit more fully from array effects, and in turn to extract wave
 614 power more efficiently.

5.8. Effect of the distance difference

615
 616 We consider the effect of varying the distances on wave power extraction from five
 617 coast-integrated OWCs subjected to incident waves with $\beta = \pi/2$. The overall length
 618 of the array is fixed as $D_1 + D_2 + D_3 + D_4 = 8h$ and the OWCs are symmetrically
 619 deployed about the central OWC, i.e., $D_1 = D_4$, $D_2 = D_3$. Seven cases with $(D_2 -$
 620 $D_1)/h = \Delta D/h = -1.5, -1.0, -0.5, 0, 0.5, 1.0$ and 1.5 are examined. Figure 17 presents the
 621 frequency responses of η_n , η and q -factor for these seven cases. Figure 17a demonstrates
 622 that for $kh \in (2.1, 2.8)$, when the second and the fourth OWCs are placed closer to the
 623 ends of the array (i.e., $\Delta D/h > 0$), more power can be captured by the two OWCs at the
 624 ends of the array compared to the uniform distribution (i.e., $\Delta D/h = 0$). Whereas when
 625 the second and the fourth OWCs are placed closer to the central OWC (i.e., $\Delta D/h < 0$),
 626 less power can be captured by the two end OWCs.

627 On the contrary, figure 17c indicates an opposite effect of $\Delta D/h$ on the power absorp-
 628 tion of the central OWC in terms of the peak value of η_3 : the peak value of η_3 is no more
 629 than 3.0 for $\Delta D/h > 0$, while it can be larger than 4.3 for each case with $\Delta D/h \leq 0$. As
 630 shown in figure 17b, the shape of the η_2 curve is significantly influenced by $\Delta D/h$. As
 631 $|\Delta D/h|$ increases from 0 to 1.5, the η_2 curve at $kh \in (1.5, 3.5)$ turns from a single peak
 632 curve into a bimodal curve. The less uniform the array layout, i.e., the larger $|\Delta D/h|$,
 633 the greater the separation between the two peaks of the curve. This is reasonable, since
 634 the hydrodynamic interaction between each pair of adjacent OWCs is dependent on the
 635 distance between them (as demonstrated in figure 15), leading to two reinforcing peaks

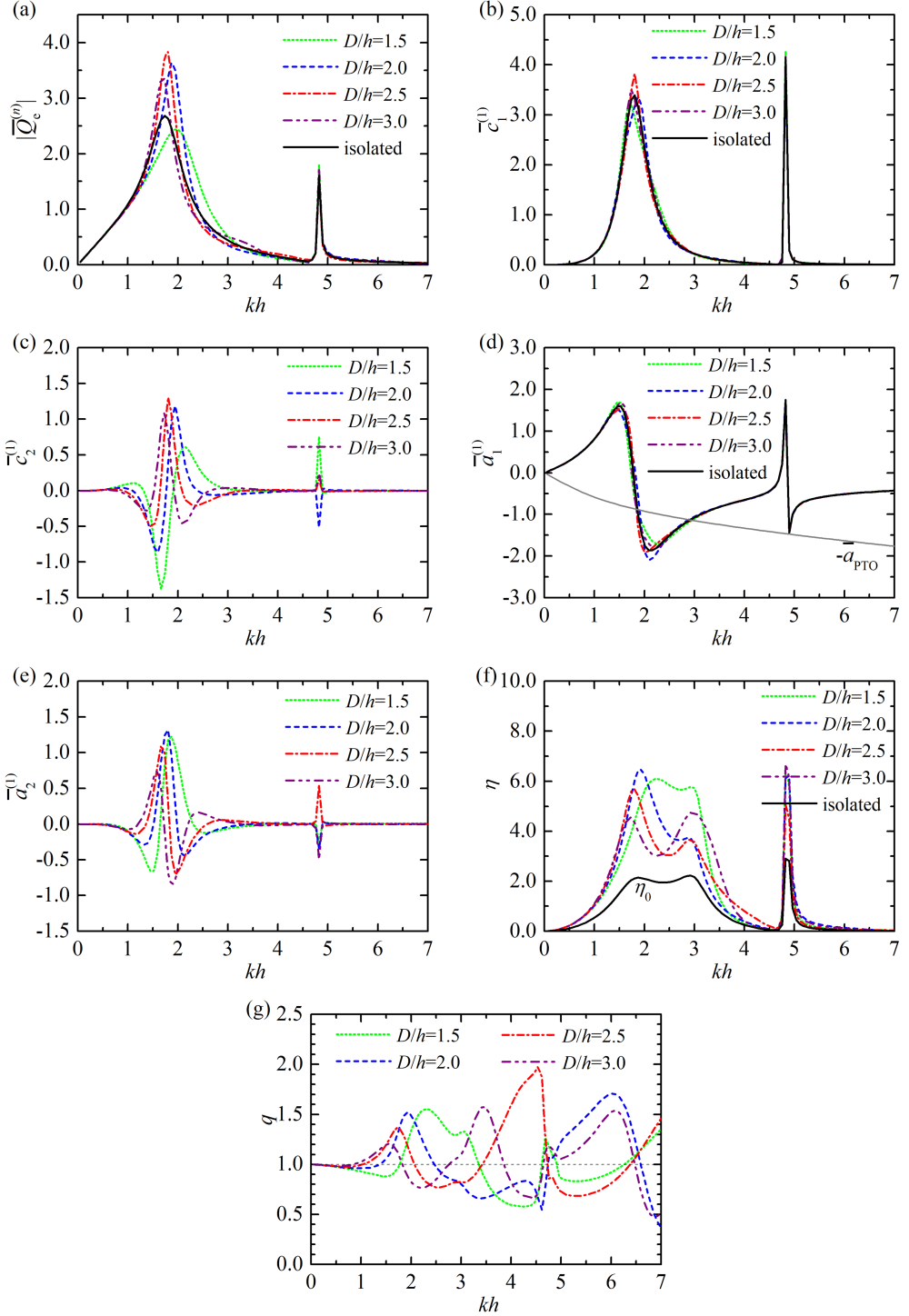


FIGURE 15. Comparison for different spacing distance between the OWCs, D/h , with $N = 2$, $R/h = 0.5$, $(R - R_i)/h = 0.1$, $d/h = 0.2$, $\beta = \pi/2$, $h = 10$ m: (a) $|\bar{Q}_c^{(n)}|$; (b) $\bar{c}_1^{(1)}$; (c) $\bar{c}_2^{(1)}$; (d) $\bar{a}_1^{(1)}$ and $-\bar{a}_{PTO}$; (e) $\bar{a}_2^{(1)}$; (f) η ; (g) q -factor.

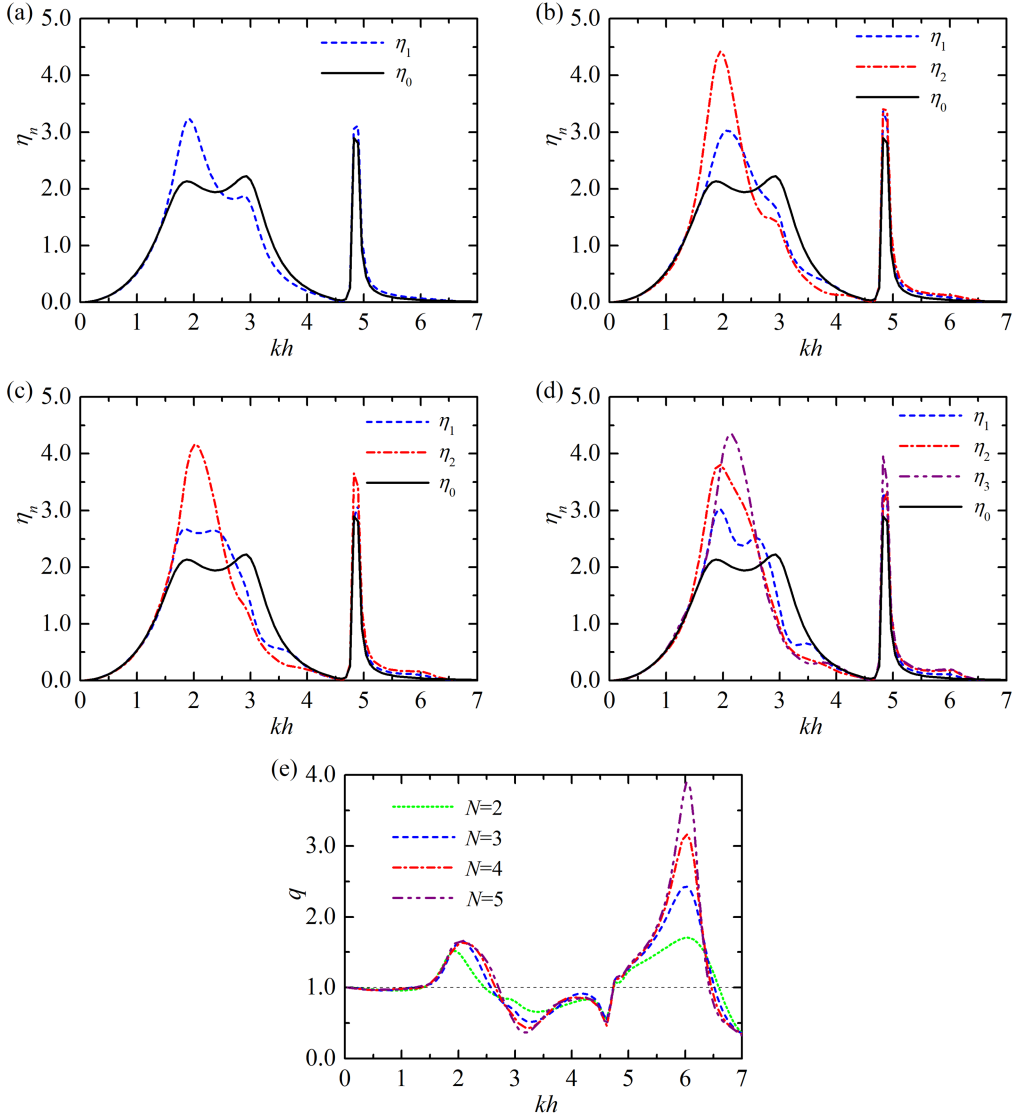


FIGURE 16. Comparison for different number of the OWCs, N , with $R/h = 0.5$, $(R-R_i)/h = 0.1$, $d/h = 0.2$, $D/h = 2.0$, $\beta = \pi/2$, $h = 10$ m: (a) η_n with $N = 2$; (b) η_n with $N = 3$; (c) η_n with $N = 4$; (d) η_n with $N = 5$; (e) q -factor.

636 of η_2 at two different frequencies when $|(D_2 - D_1)/h| = |\Delta D/h|$ is large enough. Figure
 637 17d indicates that the main peak of the total wave power capture factor of the array, η ,
 638 for $\Delta D/h = 0$ and 0.5 is larger than in other cases. Of these two options, the array with
 639 $\Delta D/h = 0.5$ might be of greater practical interest, for the power captured by each OWC
 640 is more balanced than in the case with $\Delta D/h = 0$.

641 Although the peak value of η is reduced with a non-uniform array layout, the peak
 642 is broadened. Therefore, the array with different distances may well be attractive in
 643 practice, especially for a broad-banded wave spectrum. A peak value of the q -factor
 644 larger than 2.9 is achieved for $\Delta D/h = \pm 1.5$ around $kh = 4.0$. Thanks to the constructive

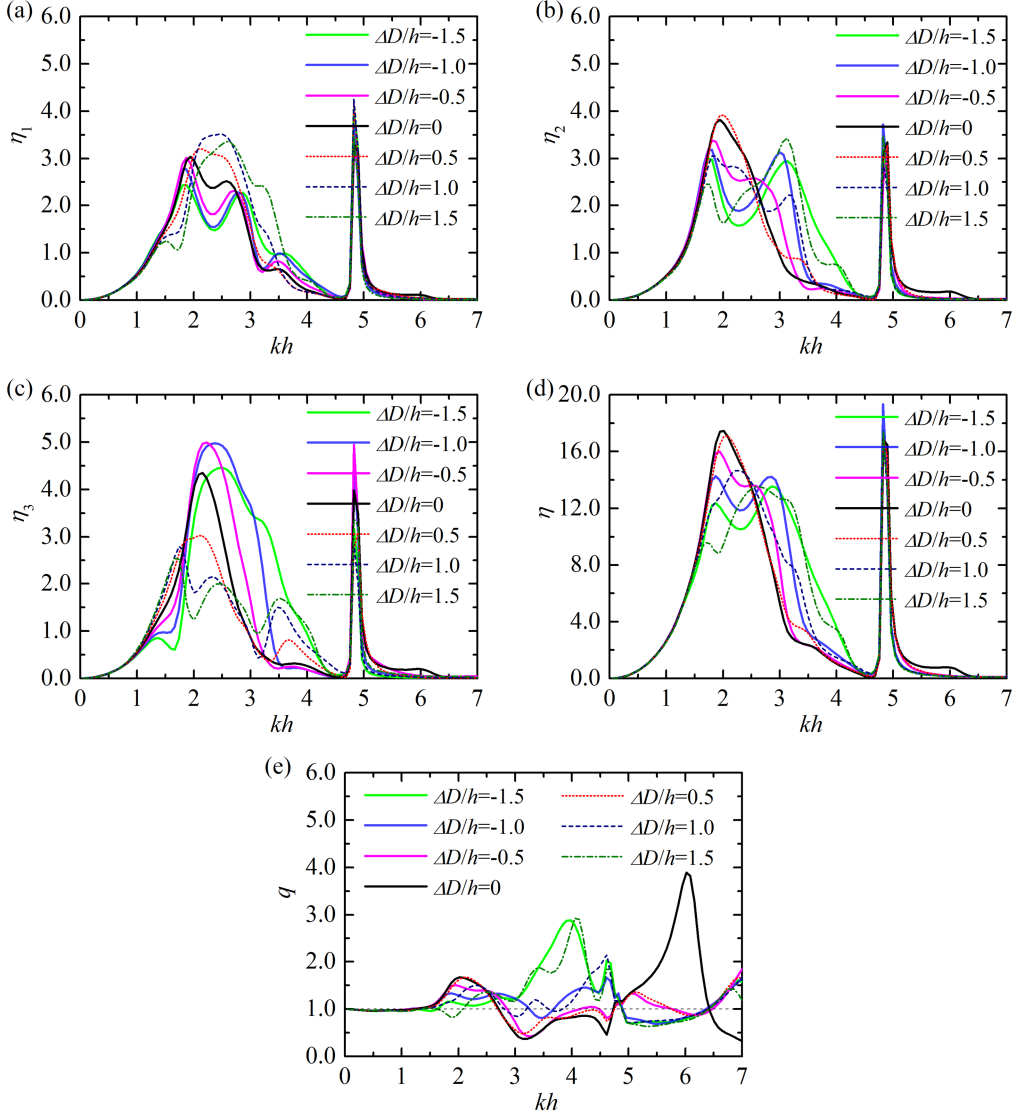


FIGURE 17. Comparison for different distance difference, $\Delta D/h$, with $N = 5$, $R/h = 0.5$, $(R - R_i)/h = 0.1$, $d/h = 0.2$, $D_1 + D_2 + D_3 + D_4 = 8h$, $D_1 = D_4$, $D_2 = D_3$, $\beta = \pi/2$, $h = 10$ m: (a) η_1 ; (b) η_2 ; (c) η_3 ; (d) η ; (e) q -factor.

645 hydrodynamic interaction, the array with $\Delta D/h = \pm 1.5$ absorbs more power than the
 646 other cases for $kh \in (3.1, 4.3)$.

647 6. Conclusions

648 An array of coast-integrated OWCs is considered in this paper. The chamber of each
 649 OWC is mainly composed of a hollow vertical circular cylinder. Each OWC cylinder is
 650 half-embedded in the wall, with the other half on the seaward side open from a finite
 651 submergence to the seabed. Based on the linear potential flow theory and eigenfunction
 652 matching method, a theoretical model was developed to solve the wave scattering and

653 wave radiation problems of these OWCs. The effects induced by the Wells turbine
 654 installed at the top of each OWC and the compressibility of air inside each chamber
 655 were represented by a linear PTO system. The present theoretical model was developed
 656 without the thin-wall restriction; hence the influence of the wall thickness of the OWC
 657 chamber on power extraction can be examined. The performances of the multiple and
 658 single coast-integrated/offshore OWCs in wave power extraction were compared with
 659 each other. The theoretical model was ultimately applied to explore the influence of the
 660 wave conditions, chamber size, spacing between the OWCs and number of OWCs on
 661 power extraction. The following conclusions may be drawn.

662 Wave reflection at the coast plays a constructive role in wave power absorption for
 663 most of the wave conditions examined. The hydrodynamic interaction between the coast-
 664 integrated OWCs, which is referred to in this work as the array effect, can enhance power
 665 extraction of the OWCs dramatically. A dramatic peak wave power capture factor, much
 666 higher than that of a single offshore/coast-integrated OWC and of multiple offshore
 667 OWCs, can be achieved due to both the constructive array effect and the constructive
 668 coast effect. For any certain wave frequency, there is a general identity, i.e., equation
 669 (5.1), of the optimum wave capture factor over all incidence angles that multiple coast-
 670 integrated OWCs must hold regardless of the OWC dimension. It means a higher peak
 671 in the curve of wave power capture factor at some incident wave directions must be
 672 associated with less power absorption at other wave incident angles.

673 As the radius of the coast-integrated OWC chambers increases, the main peaks of the
 674 frequency response curve of power capture factor shift towards lower wave frequencies
 675 and gain intensity. The wall thickness and submergence of the OWC chambers should be
 676 as small as possible to yield high wave power extraction across a broad bandwidth.

677 The spacing between two coast-integrated OWCs has a strong effect on the shape of
 678 the array factor frequency response curve as well as on its amplitude. For multiple coast-
 679 integrated OWCs with the same spacing, the one(s) closest to the central position has
 680 the highest peak power capture factor. The power absorption by individual OWCs in an
 681 array can be balanced and the frequency response of the overall wave capture factor can
 682 be improved by adopting a non-uniform array layout.

683 The linear approximation for small wave steepness was used throughout and no
 684 viscous effect was considered; hence the model is not suitable for extreme wave-structure
 685 interactions. In future work we will consider the optimization of the array from a general
 686 point of view, i.e., considering directional wave spectra, coast-integrated OWCs with
 687 different geometries (different diameters, wall thicknesses and submergences) and more
 688 elaborate PTO control strategies. “Near-trapping” effects as described by, for example,
 689 Maniar & Newman (1997); Thompson *et al.* (2008) were not registered in our results.
 690 However, this is an aspect of interest that we plan to investigate as a continuation of
 691 this line of research.

692
 693 The research was supported by Intelligent Community Energy (ICE), INTERREG
 694 V FCE, European Commission (Contract No. 5025) and the National Natural Science
 695 Foundation of China (51679124, 51879144).

696 Appendix A. Integral equations of the scattering/radiation problems

697 Inserting equations (3.1) and (3.6) into equation (3.14), after multiplying both sides
 698 by $Z_\zeta(z)e^{-i\tau\theta_n}$ and integrating for $z \in [-h, 0]$ and $\theta_n \in [0, 2\pi]$, for any pair of integers

699 (τ, ζ) , it can be shown that

$$2\pi h A_{\tau, \zeta}^{\chi, n} = \sum_{l=0}^{\infty} \left[\frac{\pi}{\varepsilon_{|\tau|}} (X_{|\tau|, l}^{(1, n)} C_{|\tau|, l}^{\chi, n} + Y_{|\tau|, l}^{(1, n)} D_{|\tau|, l}^{\chi, n}) + i \sum_{\substack{m=0 \\ m \neq |\tau|}}^{\infty} \frac{\tau [(-1)^{\tau-m} - 1]}{\tau^2 - m^2} (X_{m, l}^{(1, n)} C_{m, l}^{\chi, n} + Y_{m, l}^{(1, n)} D_{m, l}^{\chi, n}) \right] L_{l, \zeta}^{(n)}, \quad (\text{A } 1)$$

700 in which

$$X_{m, l}^{(1, n)} = \begin{cases} \frac{m}{R_n} \left(\frac{R_{i, n}}{R_n} \right)^{m-1}, & l = 0 \\ \frac{\beta_{n, l} I'_m(\beta_{n, l} R_{i, n})}{I_m(\beta_{n, l} R_n)}, & l \neq 0 \end{cases}, \quad Y_{m, l}^{(1, n)} = \begin{cases} \frac{1}{R_{i, n}}, & l = 0, m = 0 \\ -\frac{m}{R_n} \left(\frac{R_n}{R_{i, n}} \right)^{m+1}, & l = 0, m \neq 0, \\ \frac{\beta_{n, l} K'_m(\beta_{n, l} R_{i, n})}{K_m(\beta_{n, l} R_n)}, & l \neq 0 \end{cases}, \quad (\text{A } 2)$$

$$L_{l, \zeta}^{(n)} = \int_{-h}^{-d_n} \cos[\beta_{n, l}(z+h)] Z_{\zeta}(z) dz = \begin{cases} \frac{(-1)^l (h-d_n)^2 k_0 Z_0(0) \sinh[k_0(h-d_n)]}{[(h-d_n)^2 k_0^2 + l^2 \pi^2] \cosh(k_0 h)}, & \zeta = 0 \\ \frac{(-1)^l (h-d_n)^2 k_{\zeta} Z_{\zeta}(0) \sin[k_{\zeta}(h-d_n)]}{[(h-d_n)^2 k_{\zeta}^2 - l^2 \pi^2] \cos(k_{\zeta} h)}, & \zeta \neq 0 \end{cases}. \quad (\text{A } 3)$$

701 Inserting equations (3.6) and (3.13) into equation (3.15), after multiplying both sides
702 by $Z_{\zeta}(z) \cos(\tau \theta_n)$ and integrating for $z \in [-h, 0]$ and $\theta_n \in [0, \pi]$, for any pair of integers
703 (τ, ζ) , it can be shown that

$$\sum_{l=0}^{\infty} (X_{\tau, l}^{(2, n)} C_{\tau, l}^{\chi, n} + Y_{\tau, l}^{(2, n)} D_{\tau, l}^{\chi, n}) L_{l, \zeta}^{(n)} - h Z_{\tau, \zeta}^{(2, n)} E_{\tau, \zeta}^{\chi, n} - \sum_{\substack{j=1, m=0 \\ j \neq n}}^N \sum_{j \neq n}^{\infty} E_{m, \zeta}^{\chi, j} T_{m, \tau, \zeta}^{\prime n, j} = -\frac{2\delta_{\chi, 0} \delta_{\zeta, 0} \varepsilon_{\tau} \text{ig} A k_0 h}{\omega Z_0(0)} e^{-ik_0 x_n \cos \beta} (-i)^{\tau} J'_{\tau}(k_0 R_n) \cos(\tau \beta), \quad (\text{A } 4)$$

704 where

$$T_{m, \tau, \zeta}^{\prime n, j} = \frac{\varepsilon_{\tau} k_{\zeta} h \tilde{I}'_{\tau}(k_{\zeta} R_n)}{2 \tilde{K}_m(k_{\zeta} R_j)} [\tilde{K}_{m+\tau}(k_{\zeta} R_{jn}) + (-1)^{\tau \delta_{\zeta, 0}} \tilde{K}_{m-\tau}(k_{\zeta} R_{jn})] e^{i(m \alpha_{jn} + \tau \alpha_{nj})}, \quad (\text{A } 5)$$

$$X_{\tau, \zeta}^{(2, n)} = \begin{cases} \frac{\tau}{R_n}, & \zeta = 0 \\ \frac{\beta_{n, \zeta} I'_{\tau}(\beta_{n, \zeta} R_n)}{I_{\tau}(\beta_{n, \zeta} R_n)}, & \zeta \neq 0 \end{cases}, \quad Y_{\tau, \zeta}^{(2, n)} = \begin{cases} \frac{1}{R_n}, & \zeta = 0, \tau = 0 \\ -\frac{\tau}{R_n}, & \zeta = 0, \tau \neq 0, \\ \frac{\beta_{n, \zeta} K'_{\tau}(\beta_{n, \zeta} R_n)}{K_{\tau}(\beta_{n, \zeta} R_n)}, & \zeta \neq 0 \end{cases}, \quad (\text{A } 6)$$

$$Z_{\tau,\zeta}^{(2,n)} = \begin{cases} \frac{k_0 H'_\tau(k_0 R_n)}{H_\tau(k_0 R_n)}, & \zeta = 0 \\ \frac{k_\zeta K'_\tau(k_\zeta R_n)}{K_\tau(k_\zeta R_n)}, & \zeta = 1, 2, 3, \dots \end{cases} \quad (\text{A } 7)$$

705 Inserting equations (3.1) and (3.6) into equation (3.16), after multiplying both sides
706 by $\cos[\beta_{n,\zeta}(z+h)]\cos(\tau\theta_n)$ and integrating for $z \in [-h, -d_n]$ and $\theta_n \in [0, \pi]$, for any
707 pair of integers (τ, ζ) , it can be shown that

$$\begin{aligned} & \sum_{l=0}^{\infty} \left[\frac{\pi}{2} \left(\frac{\tilde{I}_\tau(k_l R_{i,n})}{k_l \tilde{I}'_\tau(k_l R_{i,n})} A_{\tau,l}^{\chi,n} + \frac{\tilde{I}_{-\tau}(k_l R_{i,n})}{k_l \tilde{I}'_{-\tau}(k_l R_{i,n})} A_{-\tau,l}^{\chi,n} \right) \right. \\ & \quad \left. - i \sum_{\substack{m=-\infty, \\ m \neq \pm\tau}}^{\infty} \frac{m[(-1)^{m-\tau} - 1]}{m^2 - \tau^2} \frac{\tilde{I}_m(k_l R_{i,n})}{k_l \tilde{I}'_m(k_l R_{i,n})} A_{m,l}^{\chi,n} \right] L_{\zeta,l}^{(n)} \\ & = \frac{\pi(h-d_n)}{\varepsilon_\tau \varepsilon_\zeta} (X_{\tau,\zeta}^{(3,n)} C_{\tau,\zeta}^{\chi,n} + Y_{\tau,\zeta}^{(3,n)} D_{\tau,\zeta}^{\chi,n}) + \frac{\delta_{\chi,n} \delta_{\tau,0} \delta_{\zeta,0} i \pi (h-d_n)}{\rho \omega}, \end{aligned} \quad (\text{A } 8)$$

708 where

$$X_{\tau,\zeta}^{(3,n)} = \begin{cases} \left(\frac{R_{i,n}}{R_n} \right)^\tau, & \zeta = 0 \\ \frac{I_\tau(\beta_{n,\zeta} R_{i,n})}{I_\tau(\beta_{n,\zeta} R_n)}, & \zeta \neq 0 \end{cases}, \quad Y_{\tau,\zeta}^{(3,n)} = \begin{cases} 1 + \ln \left(\frac{R_{i,n}}{R_n} \right), & \zeta = 0, \tau = 0 \\ \left(\frac{R_n}{R_{i,n}} \right)^\tau, & \zeta = 0, \tau \neq 0 \\ \frac{K_\tau(\beta_{n,\zeta} R_{i,n})}{K_\tau(\beta_{n,\zeta} R_n)}, & \zeta \neq 0 \end{cases}. \quad (\text{A } 9)$$

709 Inserting equations (3.6) and (3.13) into equation (3.17), after multiplying both sides
710 by $\cos[\beta_{n,\zeta}(z+h)]\cos(\tau\zeta_n)$ and integrating for $z \in [-h, -d_n]$ and $\theta_n \in [0, \pi]$, for any
711 pair of integers (τ, ζ) , the following expression is obtained

$$\begin{aligned} & \frac{h-d_n}{\varepsilon_\zeta} (C_{\tau,\zeta}^{\chi,n} + D_{\tau,\zeta}^{\chi,n}) - \sum_{l=0}^{\infty} E_{\tau,l}^{\chi,n} L_{\zeta,l}^{(n)} - \sum_{\substack{j=1, \\ j \neq n}}^N \sum_{m=0}^{\infty} \sum_{l=0}^{\infty} E_{m,l}^{\chi,j} T_{m,\tau,l}^{n,j} L_{\zeta,l}^{(n)} \\ & = - \frac{2\delta_{\chi,0} \varepsilon_\tau i g A L_{\zeta,0}^{(n)}}{\omega Z_0(0)} e^{-ik_0 x_n \cos \beta} (-i)^\tau J_\tau(k_0 R_n) \cos(\tau\beta), \end{aligned} \quad (\text{A } 10)$$

712 in which

$$T_{m,\tau,l}^{n,j} = \frac{\varepsilon_\tau \tilde{I}_\tau(k_l R_n)}{2\tilde{K}_m(k_l R_j)} [\tilde{K}_{m+\tau}(k_l R_{jn}) + (-1)^{\tau\delta_{l,0}} \tilde{K}_{m-\tau}(k_l R_{jn})] e^{i(m\alpha_{jn} + \tau\alpha_{nj})}. \quad (\text{A } 11)$$

713 A linear algebraic system can be formed by equations (A 1), (A 4), (A 8) and (A 10),
714 and can be used to solve the unknown coefficients $A_{m,l}^{\chi,n}$, $C_{m,l}^{\chi,n}$, $D_{m,l}^{\chi,n}$ and $E_{m,l}^{\chi,n}$ numerically
715 after truncation. In the present model, the infinite terms of $e^{-im\theta_n}/\cos(m\theta_n)$ and
716 $Z_l(z)/\cos[\beta_{n,l}(z+h)]$ are truncated at $m = M$ and $l = L$, respectively. Accurate results
717 can be obtained by choosing $M = 12$ and $L = 20$.

718 **Appendix B. Identity of optimum wave capture factor over all**
 719 **incidence angles**

720 Following Evans (1980); Falnes (1980), the theoretical maximum power that may be
 721 extracted by multiple coast-integrated OWCs can be expressed as

$$P_{\text{MAX}} = \frac{1}{8} \mathbf{Q}_e^\dagger(\beta) \mathbf{C}^{-1} \mathbf{Q}_e(\beta), \quad (\text{B } 1)$$

722 which is obtained when an ideal PTO system is applied, such that

$$\mathbf{p}(\beta) = \mathbf{p}_{\text{opt}}(\beta) = \frac{1}{2} \mathbf{C}^{-1} \mathbf{Q}_e(\beta) \quad (\text{B } 2)$$

723 is satisfied (provided \mathbf{C} is non-singular).

724 Note that \mathbf{C} is composed of real elements, and, more specifically, it can be shown from
 725 equation (3.20) that \mathbf{C} is symmetric. Assuming \mathbf{C} is positive definite (Wolgamot *et al.*
 726 2012), \mathbf{C} can be written as the product of an upper real triangular matrix \mathbf{H} and its
 727 transpose with the employment of the Cholesky decomposition,

$$\mathbf{C} = \mathbf{H}^T \mathbf{H}, \quad (\text{B } 3)$$

728 where T denotes the conjugate transpose. Hence,

$$\mathbf{C}^{-1} = \mathbf{H}^{-1} (\mathbf{H}^T)^{-1}. \quad (\text{B } 4)$$

729 For the sake of convenience, a column vector of length N is defined as (Wolgamot *et*
 730 *al.*, 2012)

$$\mathbf{S}(\beta) = (\mathbf{H}^T)^{-1} \mathbf{Q}_e(\beta), \quad (\text{B } 5)$$

731 from which equation (B 1) can be rewritten as

$$P_{\text{MAX}}(\beta) = \frac{1}{8} \mathbf{S}^\dagger(\beta) \mathbf{S}(\beta). \quad (\text{B } 6)$$

732 Rewriting (3.20) in the matrix format gives

$$\mathbf{C} = \frac{k}{8\pi\rho g c_g A^2} \int_0^\pi \mathbf{Q}_e(\beta) \mathbf{Q}_e^\dagger(\beta) d\beta. \quad (\text{B } 7)$$

733 Multiplying two \mathbf{H} related inverse matrices results in

$$(\mathbf{H}^T)^{-1} \mathbf{C} \mathbf{H}^{-1} = \frac{k}{8\pi\rho g c_g A^2} \int_0^\pi \mathbf{S}(\beta) \mathbf{S}^\dagger(\beta) d\beta = \mathbf{I}, \quad (\text{B } 8)$$

734 leading to the integral

$$\int_0^\pi S_i(\beta) S_j^*(\beta) d\beta = \delta_{i,j} \frac{8\pi\rho g c_g A^2}{k}. \quad (\text{B } 9)$$

735 Integrating equation (B 6) over $\beta \in [0, \pi]$ and adopting equation (B 9) gives

$$\int_0^\pi P_{\text{MAX}} d\beta = \frac{N\pi\rho g c_g A^2}{k}, \quad (\text{B } 10)$$

736 and

$$\frac{1}{\pi} \int_0^\pi \eta_{\text{MAX}}(\beta) d\beta = \frac{2k}{\pi\rho g c_g A^2} \int_0^\pi P_{\text{MAX}}(\beta) d\beta = 2N. \quad (\text{B } 11)$$

- 737 ABRAMOWITZ, M. & STEGUN, I. A. 1964 *Handbook of mathematical functions*. Washington,
738 D.C.: Government Printing Office.
- 739 ARENA, F., ROMOLO, A., MALARA, G., FIAMMA, V. & LAFACE, V. 2017 The first full
740 operative U-OWC plants in the port of civitavecchia. In *ASME 2017 36th International*
741 *Conference on Ocean, Offshore and Arctic Engineering*, p. V010T09A022. American
742 Society of Mechanical Engineers.
- 743 ASTARIZ, S. & IGLESIAS, G. 2015 The economics of wave energy: A review. *Renewable and*
744 *Sustainable Energy Reviews* **45**, 397–408.
- 745 BOCCOTTI, P. 2007 Caisson breakwaters embodying an OWC with a small opening-part I:
746 Theory. *Ocean Engineering* **34** (5-6), 806–819.
- 747 CLÉMENT, A., MCCULLEN, P., FALCÃO, A. F. DE O., FIORENTINO, A., GARDNER, F.,
748 HAMMARLUND, K., LEMONIS, G., LEWIS, T., NIELSEN, K., PETRONCINI, S., PONTES,
749 M. T., SCHILD, P., SJÖSTRÖM, B. O., SØRENSEN, H. C. & THORPE, T. 2002 Wave
750 energy in Europe: current status and perspectives. *Renewable and Sustainable Energy*
751 *Reviews* **6** (5), 405 – 431.
- 752 DI LAURO, E., LARA, J. L., MAZA, M., LOSADA, I. J., CONTESTABILE, P. & VICINANZA,
753 D. 2019 Stability analysis of a non-conventional breakwater for wave energy conversion.
754 *Coastal Engineering* **145**, 36–52.
- 755 DREW, B., PLUMMER, A. R. & SAHINKAYA, M. N. 2009 A review of wave energy converter
756 technology. *Proceedings of the Institution of Mechanical Engineers Part A-Journal of*
757 *Power and Energy* **223** (A8), 887–902.
- 758 ELHANAFI, A., FLEMING, A., MACFARLANE, G. & LEONG, Z. 2016 Numerical energy balance
759 analysis for an onshore oscillating water column–wave energy converter. *Energy* **116**, 539–
760 557.
- 761 ELHANAFI, A., FLEMING, A., MACFARLANE, G. & LEONG, Z. 2017 Underwater geometrical
762 impact on the hydrodynamic performance of an offshore oscillating water column–wave
763 energy converter. *Renewable Energy* **105**, 209–231.
- 764 EVANS, D. V. 1980 *Some analytic results for two-and three-dimensional wave-energy absorbers*.
765 London: Academic Press.
- 766 EVANS, D. V. 1988 The maximum efficiency of wave-energy devices near coast lines. *Applied*
767 *Ocean Research* **10** (3), 162 – 164.
- 768 EVANS, D. V. & PORTER, R. 1995 Hydrodynamic characteristics of an oscillating water column
769 device. *Applied Ocean Research* **17** (3), 155–164.
- 770 FALCÃO, A. F. DE O. & HENRIQUES, J. C. C. 2016 Oscillating-water-column wave energy
771 converters and air turbines: A review. *Renewable Energy* **85**, 1391–1424.
- 772 FALCÃO, A. F. DE O., HENRIQUES, J. C. C. & GATO, L. M. C. 2016 Air turbine optimization
773 for a bottom-standing oscillating-water-column wave energy converter. *Journal of Ocean*
774 *Engineering and Marine Energy* **2** (4), 459–472.
- 775 FALNES, J. 1980 Radiation impedance matrix and optimum power absorption for interacting
776 oscillators in surface waves. *Applied Ocean Research* **2** (2), 75–80.
- 777 FALNES, J. 2002 *Ocean waves and oscillating systems: linear interactions including wave-energy*
778 *extraction*. Cambridge university press.
- 779 HE, F., HUANG, Z. & LAW, A. W. K. 2012 Hydrodynamic performance of a rectangular
780 floating breakwater with and without pneumatic chambers: An experimental study. *Ocean*
781 *Engineering* **51**, 16–27.
- 782 HE, F., LENG, J. & ZHAO, X. 2017 An experimental investigation into the wave power extraction
783 of a floating box-type breakwater with dual pneumatic chambers. *Applied Ocean Research*
784 **67**, 21–30.
- 785 HE, F., ZHANG, H., ZHAO, J., ZHENG, S. & IGLESIAS, G. 2019 Hydrodynamic performance of
786 a pile-supported OWC breakwater: An analytical study. *Applied Ocean Research* **88**, 326
787 – 340.
- 788 HEATH, T. V. 2012 A review of oscillating water columns. *Philosophical Transactions of the*
789 *Royal Society A: Mathematical, Physical and Engineering Sciences* **370** (1959), 235–245.
- 790 HENRIQUES, J. C. C., GATO, L. M. C., FALCÃO, A. F. DE O., ROBLES, E. & FAÏ, F. X. 2016
791 Latching control of a floating oscillating-water-column wave energy converter. *Renewable*
792 *Energy* **90**, 229–241.
- 793 HERAS-SAZARBITORIA, I., ZAMANILLO, I. & LASKURAIN, I. 2013 Social acceptance of ocean

- 794 wave energy: A case study of an OWC shoreline plant. *Renewable and Sustainable Energy*
795 *Reviews* **27**, 515–524.
- 796 HOWE, D. & NADER, J. R. 2017 OWC WEC integrated within a breakwater versus isolated:
797 Experimental and numerical theoretical study. *International Journal of Marine Energy*
798 **20**, 165–182.
- 799 KONISPOLIATIS, D. N. & MAVRAKOS, S. A. 2016 Hydrodynamic analysis of an array of
800 interacting free-floating oscillating water column (OWC's) devices. *Ocean Engineering*
801 **111**, 179–197.
- 802 KURNIAWAN, A., CHAPLIN, J. R., GREAVES, D. M. & HANN, M. 2017 Wave energy absorption
803 by a floating air bag. *Journal of Fluid Mechanics* **812**, 294–320.
- 804 LÓPEZ, I., CARBALLO, R., TAVEIRA-PINTO, F. & IGLESIAS, G. 2019 Sensitivity of owc
805 performance to air compressibility. *Renewable Energy in press*.
- 806 LÓPEZ, I. & IGLESIAS, G. 2014 Efficiency of OWC wave energy converters: A virtual laboratory.
807 *Applied Ocean Research* **44**, 63–70.
- 808 LÓPEZ, I., PEREIRAS, B., CASTRO, F. & IGLESIAS, G. 2014 Optimisation of turbine-induced
809 damping for an OWC wave energy converter using a RANS–VOF numerical model.
810 *Applied Energy* **127**, 105–114.
- 811 LÓPEZ, I., PEREIRAS, B., CASTRO, F. & IGLESIAS, G. 2016 Holistic performance analysis
812 and turbine-induced damping for an OWC wave energy converter. *Renewable Energy* **85**,
813 1155–1163.
- 814 LOVAS, S., MEI, C. C. & LIU, Y. 2010 Oscillating water column at a coastal corner for wave
815 power extraction. *Applied Ocean Research* **32** (3), 267–283.
- 816 MANIAR, H. D. & NEWMAN, J. N. 1997 Wave diffraction by a long array of cylinders. *Journal*
817 *of Fluid Mechanics* **339**, 309330.
- 818 MARTINS-RIVAS, H. & MEI, C. C. 2009a Wave power extraction from an oscillating water
819 column along a straight coast. *Ocean Engineering* **36** (6-7), 426–433.
- 820 MARTINS-RIVAS, H. & MEI, C. C. 2009b Wave power extraction from an oscillating water
821 column at the tip of a breakwater. *Journal of Fluid Mechanics* **626**, 395–414.
- 822 MICHELE, S., SAMMARCO, P. & D'ERRICO, M. 2016 The optimal design of a flap gate array in
823 front of a straight vertical wall: Resonance of the natural modes and enhancement of the
824 exciting torque. *Ocean Engineering* **118**, 152 – 164.
- 825 MORRIS-THOMAS, M. T., IRVIN, R. J. & THIAGARAJAN, K. P. 2007 An investigation into the
826 hydrodynamic efficiency of an oscillating water column. *Journal of Offshore Mechanics*
827 *and Arctic Engineering* **129** (4), 273–278.
- 828 MUSTAPA, M. A., YAAKOB, O. B., AHMED, Y. M., RHEEM, C. K., KOH, K. K. & ADNAN,
829 F. A. 2017 Wave energy device and breakwater integration: A review. *Renewable and*
830 *Sustainable Energy Reviews* **77**, 43–58.
- 831 NADER, J. R., ZHU, S. P. & COOPER, P. 2014 Hydrodynamic and energetic properties of a
832 finite array of fixed oscillating water column wave energy converters. *Ocean Engineering*
833 **88**, 131–148.
- 834 NADER, J. R., ZHU, S. P., COOPER, P. & STAPPENBELT, B. 2012 A finite-element study of the
835 efficiency of arrays of oscillating water column wave energy converters. *Ocean Engineering*
836 **43**, 72–81.
- 837 NIHOUS, G. C. 2012 Wave power extraction by arbitrary arrays of non-diffracting oscillating
838 water columns. *Ocean Engineering* **51**, 94–105.
- 839 NING, D., ZHOU, Y. & ZHANG, C. 2018 Hydrodynamic modeling of a novel dual-chamber OWC
840 wave energy converter. *Applied Ocean Research* **78**, 180–191.
- 841 PAWITAN, K. A., DIMAKOPOULOS, A. S., VICINANZA, D., ALLSOP, W. & BRUCE, T. 2019
842 A loading model for an OWC caisson based upon large-scale measurements. *Coastal*
843 *Engineering* **145**, 1–20.
- 844 PEREIRAS, B., LÓPEZ, I., CASTRO, F. & IGLESIAS, G. 2015 Non-dimensional analysis for
845 matching an impulse turbine to an OWC (oscillating water column) with an optimum
846 energy transfer. *Energy* **87**, 481–489.
- 847 RUSU, E. & ONEA, F. 2018 A review of the technologies for wave energy extraction. *Clean*
848 *Energy* **2** (1), 10–19.
- 849 SARKAR, D., RENZI, E. & DIAS, F. 2015 Effect of a straight coast on the hydrodynamics and
850 performance of the Oscillating Wave Surge Converter. *Ocean Engineering* **105**, 25 – 32.

- 851 SARMENTO, A. J. N. A. & FALCÃO, A. F. DE O. 1985 Wave generation by an oscillating surface-
852 pressure and its application in wave-energy extraction. *Journal of Fluid Mechanics* **150**,
853 467485.
- 854 SHENG, W. & LEWIS, A. 2018 Power takeoff optimization to maximize wave energy conversions
855 for oscillating water column devices. *IEEE Journal of Oceanic Engineering* **43** (1), 36–47.
- 856 THOMPSON, I., LINTON, C. M. & PORTER, R. 2008 A new approximation method for scattering
857 by long finite arrays. *The Quarterly Journal of Mechanics & Applied Mathematics* **61** (3),
858 333–352.
- 859 VIVIANO, A., NATY, S., FOTI, E., BRUCE, T., ALLSOP, W. & VICINANZA, D. 2016 Large-scale
860 experiments on the behaviour of a generalised oscillating water column under random
861 waves. *Renewable Energy* **99**, 875 – 887.
- 862 WOLGAMOT, H. A., TAYLOR, P. H. & TAYLOR, R. EATOCK 2012 The interaction factor and
863 directionality in wave energy arrays. *Ocean Engineering* **47**, 65 – 73.
- 864 YU, H., ZHENG, S., ZHANG, Y. & IGLESIAS, G. 2019 Wave radiation from a truncated cylinder
865 of arbitrary cross section. *Ocean Engineering* **173**, 519 – 530.
- 866 ZHANG, C. & NING, D. 2019 Hydrodynamic study of a novel breakwater with parabolic openings
867 for wave energy harvest. *Ocean Engineering* **182**, 540 – 551.
- 868 ZHANG, Y., ZOU, Q. P. & GREAVES, D. 2012 Airwater two-phase flow modelling of
869 hydrodynamic performance of an oscillating water column device. *Renewable Energy* **41**,
870 159 – 170.
- 871 ZHAO, X., NING, D., JOHANNING, L. & TENG, B. 2018 Numerical investigation on
872 hydrodynamic performance of a wec array integrated into a pontoon. In *The 28th*
873 *International Ocean and Polar Engineering Conference*. International Society of Offshore
874 and Polar Engineers.
- 875 ZHENG, S. & ZHANG, Y. 2015 Wave diffraction from a truncated cylinder in front of a vertical
876 wall. *Ocean Engineering* **104**, 329 – 343.
- 877 ZHENG, S. & ZHANG, Y. 2016 Wave radiation from a truncated cylinder in front of a vertical
878 wall. *Ocean Engineering* **111**, 602 – 614.
- 879 ZHENG, S. & ZHANG, Y. 2018 Theoretical modelling of a new hybrid wave energy converter in
880 regular waves. *Renewable Energy* **128**, 125 – 141.
- 881 ZHENG, S., ZHANG, Y. & IGLESIAS, G. 2018 Wave-structure interaction in hybrid wave farms.
882 *Journal of Fluids and Structures* **83**, 386 – 412.
- 883 ZHENG, S., ZHANG, Y. & IGLESIAS, G. 2019 Coast/breakwater-integrated OWC: A theoretical
884 model. *Marine Structures* **66**, 121 – 135.